MASSIVE LYMAN BREAK GALAXIES AT $Z \sim 3$ IN THE *SPITZER* EXTRAGALACTIC FIRST LOOK SURVEY

HYUNJIN SHIM[1], MYUNGSHIN IM[1], PHILLIP CHOI[2], LIN YAN[3], & LISA STORRIE-LOMBARDI[3]

Draft version February 1, 2008

ABSTRACT

We investigate the properties of 1088 Lyman Break Galaxies (LBGs) at $z \sim 3$ selected from a ~ 2.63 deg^2 sub-region of the First Look Survey field using the ground-based multi-color data and the Spitzer Space Telescope mid-infrared data at 3–8 and 24 μm. With the wide area and the broad wavelength coverage, we sample a large number of "rare" u-band dropouts which are massive ($M_* > 10^{11} M_\odot$), allowing us to perform a statistical analysis of these subsets of LBGs that have not been studied in detail. Optically bright ($R_{AB} \leq 24.5$ mag) LBGs detected in mid-infrared ($S_{3.6\mu m} \geq 6\mu$Jy) reside at the most massive and dusty end of the LBG population, with relatively high and tight M/L in rest-frame near-infrared. Most infrared-luminous LBGs ($S_{24\mu m} \geq 100\mu$Jy) are dusty star-forming galaxies with star formation rates of 100–1000 $M_\odot$/yr, total infrared luminosity of $> 10^{12} L_\odot$. By constructing the UV luminosity function of massive LBGs, we estimate that the lower limit for the star formation rate density from LBGs more massive than $10^{11} M_\odot$ at $z \sim 3$ is $\geq 3.3 \times 10^{-3} M_\odot/yr/Mpc^3$, showing for the first time that the UV-bright population of massive galaxies alone contributes significantly to the global star formation rate density at $z \sim 3$. When combined with the star formation rate densities at $z < 2$, our result reveals a steady increase in the contribution of massive galaxies to the global star formation from $z = 0$ to $z \sim 3$, providing strong support to the downsizing of galaxy formation.

Subject headings: cosmology: observations – galaxies: evolution – galaxies: high-redshift – galaxies: stellar content – galaxies: starburst – infrared: galaxies

1. INTRODUCTION

Stellar population analysis of local galaxies shows that stars in massive galaxies formed early within a short period in the history of the universe, while low-mass galaxies went through late, slow star formation (Thomas et al. 2005; Heavens et al. 2004; Panter et al. 2006). The appearance of passively evolving early-type galaxies above $z \geq 1$ (Cimatti et al. 2002; Förster-Schreiber et al. 2004) supports the idea of early star formation in massive systems. The evolution of specific star formation rate, i.e., the star formation rate per unit stellar mass shows that the star formation in most massive galaxies ($M_* \gtrsim 10^{11} M_\odot$) have nearly completed by $z \sim 1.5$ while that for less massive galaxies continue to date (Papovich et al. 2006). These observations support the "downsizing" scenario of galaxy formation, commonly expressed as the decrease of stellar masses of galaxies in which vigorous star formation occurs with decreasing redshift (Cowie et al. 1996; Kodama et al. 2004; Juneau et al. 2005).

Attempts have been made to explain this seemingly anti-hierarchical behavior of galaxy formation using hierarchical galaxy formation models. In an attempt to explain downsizing within the frame of semi-analytic model, Neistein, van den Bosch, and Dekel (2006) distinguishes "archaeological downsizing "(ADS) versus "downsizing in time"(DST). In ADS, the downsizing is characterized as the built-up of stellar masses where massive galaxies are assembled through mergers of less massive galaxies which formed stars early. In comparison, DST is characterized by the formation and assembly of massive systems at early epoch. Semi-analytical models seem to be able to explain ADS naturally, while complicated baryonic processes are necessary to explain DST. Recent semi-analytic models have shown that the inclusion of

AGN feedback effect successfully reproduce the observed decrease of actively star-forming system, yet more understanding about the observed quantities and cooling processes are needed. On the other hand, some other models do not seem to have much difficulty explaining the abundance of massive galaxies at high redshift (e.g., Nagamine et al. 2005).

Recent observational evidences point toward the DST-type of downsizing which suggests that there should be "massive", star-forming galaxies at high redshift. Some of the red, massive galaxies are found to be dusty star-forming galaxies, and submm galaxies are thought to be massive galaxies in formation at high redshift (Smail et al. 2002). Still, it is not clear if they account for the whole star formation activity of massive galaxies. To complete the picture of the downsizing galaxy formation and to provide additional constraints to refine the models, we need to identify and study other actively star-forming massive galaxies, such as Lyman break galaxies (LBGs).

Lyman break galaxies, galaxies selected by the continuum break at the Lyman limit, are the most commonly studied high-redshift star-forming galaxies. Since their selection technique requires only optical imaging observation, many LBGs up to $z \sim 6$ have been discovered and studied to date (Steidel et al. 1999; Papovich et al. 2001; Shapley et al. 2001; Giavalisco 2002; Ouchi et al. 2004; Bouwens et al. 2004). These studies reveal that typical $z \sim 3$ LBGs are galaxies with large ongoing star formation of 10–100 $M_\odot$/yr (Papovich et al. 2001; Shapley et al. 2001). Typical stellar masses of $z \sim 3$ LBGs are found to be mostly of order of $10^{10} M_\odot$ or less from the spectral energy distribution fitting using optical and near-infrared photometry, although LBGs with masses up to $10^{11} M_\odot$ were also found (Papovich et al. 2001; Shapley et al. 2001). Some simulations suggest that nearly 50% of $\geq 10^{11} M_\odot$ galaxies could be detected using the rest-frame UV selection criteria (Nagamine et al. 2005), but the observed fraction of LBGs among massive galaxies is less than 20% (van Dokkum et al. 2006).

[1] Department of Physics & Astronomy, FPRD, Seoul National University, Seoul, Korea ; hjshim@astro.snu.ac.kr, mim@astro.snu.ac.kr
[2] Department of Physics & Astronomy, Pomona College, CA91711
[3] Spitzer Science Center, California Institute of Technology, CA91125

Recently, the addition of *Spitzer* mid-infrared (MIR) observations not only reduced the uncertainties in derivation of stellar mass (Shapley et al. 2005), but also enabled the estimation of the infrared luminosities of LBGs. Huang et al.(2005) have defined Infrared Luminous LBGs (ILLBGs) as LBGs detected in the *Spitzer* MIPS 24 μm with $f_{24\mu m} > 60\mu$Jy. The infrared luminosities of ILLBGs are estimated to be larger than $10^{12}L_\odot$, and they contribute $\sim 5\%$ of total LBG population. The stellar masses of ILLBGs exceed $5 \times 10^{10}M_\odot$ (Rigopoulou et al. 2006), and their star formation rates inferred from infrared luminosity are as high as $\sim 1000M_\odot$/yr that is sufficient to evolve into present-day giant ellipticals. Several massive LBGs, not necessarily ILLBGs, are also identified in a part of the Extended Groth Strip covering ~ 227 arcmin^2 (Rigopoulou et al. 2006). These massive LBGs are found to have a star formation rate (SFR) of $\gtrsim 100M_\odot$/yr. These results suggest that ILLBGs and massive LBGs are important indicators of the star formation activity in massive galaxies at high redshift, along with the distant red galaxies (DRGs; Franx et al. 2003) and the submm galaxies.

However, the number of $z \sim 3$ massive LBGs and ILLBGs is still small due to the difficulty of covering large areas with expensive *u*-band observations in order to discover such rare objects. For example, only 5 massive ($> 10^{11}M_\odot$) LBGs are found in Rigopoulou et al.(2006). At $z \sim 3$, the largest LBG sample (2347 photometric LBGs) until now is gathered from 11 separate fields of ~ 0.38 deg^2 in total (Steidel et al. 2003). LBGs selected in the ESO Deep Public Survey (Hildebrandt et al. 2007) covers as much as ~ 1.75 deg^2 at bright end ($30' \times 30' \times 7$; $R_{AB} \leq 24.0$), but until now, the survey consists of optical data only.

In this study, we enlarge the $z \sim 3$ massive LBG/ILLBG sample and investigate their properties using *Spitzer* First Look Survey. The survey is not as deep as other multiwavelength surveys, however, it is wide enough (~ 4.3 deg^2, of which 2.63 deg^2 was used in this study) to collect the rare bright LBGs. LBGs selected in optical bands (with *R*-band magnitude cut of $R_{AB} \leq 24.5$ mag) are combined with detections in *Spitzer* IRAC (3.6–8μm) and MIPS (24μm). By comparing observed flux with model galaxy spectra, we estimate ages, the amount of dust extinction, and stellar masses of the LBGs. We also present 24μm detected LBGs in our study, and compare them with the ILLBGs in Huang et al.(2005).

The data set we used is described in §2. We describe our selection criteria for $z \sim 3$ LBG candidates in §3. The analysis on the stellar population of LBGs follows in §4, and the key results are presented in §5, such as the luminosity function, the stellar mass properties, and dust properties. We also discuss the implication of our study on the galaxy evolution, in particular regarding the "downsizing" picture of galaxy formation in §5. Finally in §6, the conclusion follows. Throughout this paper, we use a cosmology with $\Omega_M = 0.3$, $\Omega_\Lambda = 0.7$, and $H_0 = 70 km/s/Mpc$. All the magnitudes are specified in AB system, unless noted.

2. DATA

The LBG candidates are selected from the extragalactic component of the *Spitzer* First Look Survey (XFLS). XFLS comprises of InfraRed Array Camera (IRAC, 3.6, 4.5, 5.8, 8.0μm; Fazio et al. 2004) and Multiband Imaging Photometer for Spitzer (MIPS, 24, 70, 160μm; Rieke et al. 2004) imaging observations over the ~ 4.3 deg^2 field centered at RA= $17^h18^m00^s$, DEC= $+59°30'00''$. With an effective exposure time of 1 minute per pixel, the main survey field (~ 4.3
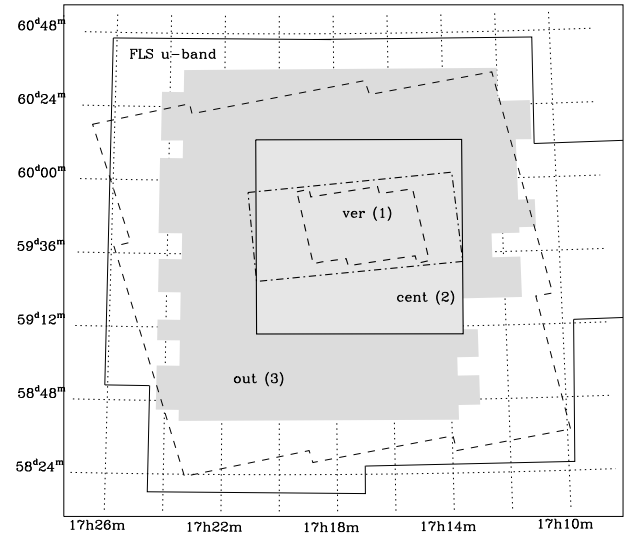

FIG. 1.— The area coverage maps of various datasets in XFLS. The smallest region marked with thick*dashed* line in the center represents verification field for IRAC (~ 900 arcmin^2) that is slightly deeper than other parts of XFLS. The skewed rectangle (*dash-dot-dash* line) is the MIPS verification strip. The "central 1 deg^2" region is drawn as a thick square in the center. The shaded area outside the central 1 deg^2 region represents the outer field (~ 1.63 deg^2) where bright *u*-dropouts are selected. The IRAC main field of XFLS is specified with the thin *dashed* line at outermost. Thin *Solid* line shows our *u*-band coverage.

deg^2) has 5 σ flux limits of 20, 25, 100, and 100μJy at wavelengths of IRAC 3.6, 4.5, 5.8, and 8.0μm respectively. The flux limit of MIPS 24μm is about $\sim 300\mu$Jy (5 σ). The central part of the FLS (~ 900 arcmin^2) was observed deeper, with 10-minute integration times per pixel. This "verification" field has sensitivities of 10, 10, 30, and 30μJy at IRAC wavelengths (5 σ; Lacy et al. 2005). For the MIPS verification field, 3 σ flux limits are 90μJy at 24μm (Fadda et al. 2006), 9 and 60 mJy at 70 and 160μm respectively (Frayer et al. 2006).

In order to select *u*-dropout objects in the XFLS, we used *u*, *g*, and *R*-band ground-based images acquired by three different wide-field instruments. We obtained deep u^*-band images with MegaCam on the Canada-France-Hawaii Telescope (CFHT) 3.6-m telescope (Shim et al. 2006). CFHT u^*-band filters are slightly redder than popular SDSS *u*-band. Therefore using the similar color selection criteria, we expect that the u^*-band dropouts are biased towards higher-redshift objects than previously selected LBGs. The central 1 deg^2 field was observed to the depth of $u^* \sim 26.2$ mag (AB, 5σ in 3$''$ diameter aperture). In addition to the central part, the whole FLS area was covered by u^*-band imaging with a shallower depth (~ 24.5 mag). Detailed information about the observations, photometry and the properties of the dataset are presented in a separate paper (Shim et al. 2006). Deep *g*-band image was obtained together with the u^*-band observation over the central 1 deg^2 ($g \sim 26.5$ mag).

The g'-band images were obtained over ~ 2.63 deg^2, including the central 1 deg^2 area, using Large Format Camera (LFC; Simcoe et al. 2000) at the Palomar 5-m telescope (Storrie-Lombardi et al., in preparation). The LFC g'-band images reach to the depth of 24.5 mag. For the re-

gion surrounding the central 1 deg^2 area, we use the LFC data for g-band photometry. The u^*, g catalogs were extracted through dual-mode photometry of SExtractor (Bertin & Arnouts 1996), using the g-band image as a reference image. The R-band catalog of the FLS (Fadda et al. 2004) were matched with u^*, g-band catalogs using the matching radius of $0.8''$, to obtain the R-band flux. The depth of the R-band image varies depending on the field location. Still, it reaches $R(Vega) \sim 24.5$ mag at the deepest central field. Our method to select $z \sim 3$ LBGs with optical colors is described in detail in Section 3.

Other ancillary datasets used to investigate the properties of u-dropout objects include i', J, and K_s-band images. LFC i'-band images cover the same area with the LFC g'-band images with the depth of ~ 24 mag. For the central part less than 1 deg^2, we also used NIR ($J(Vega) \sim 21$ mag, $K_s(Vega) \sim 20$–21 mag) data, obtained with WIRC on the Palomar 5-m (K_s-band), and FLAMINGOS on the KPNO 4-m (J-band; Choi et al., in preparation). The whole FLS field was covered by 1.4 GHz radio observations with VLA (flux limit at 90 μJy, Condon et al. 2003). In this study, spectroscopic redshifts acquired with DEIMOS/Keck for $\sim$1300 objects at $z \sim 1$ (Choi et al. 2006) were used to check if there is any low-redshift interlopers within the LBG sample.

3. LBG SAMPLE SELECTION

3.1. *Photometric Selection Criteria for u-dropouts*

We select u-dropout objects from the 2.63 deg^2 area that is covered by u^*, g, R, and i-bands. This area is illustrated as a shaded region in Figure 1. We define u-dropouts as objects that satisfy R-band magnitude cut and color-cut criteria in $g-R$ versus u^*-g diagram. The method is in principle identical to the popular "drop-out" method for selecting LBGs (e.g., Steidel & Hamilton, 1993).

The adopted selection criteria can be summarized as follows:

$$u-g \geq 1.4,$$
$$u-g \geq 3(g-R)-0.12,$$
$$g-R \leq 1.2,$$
$$R \leq 24.5 \text{ (for central 1 deg}^2\text{)}, R \leq 23.5 \text{ (for the outer area)}$$

Different R-band magnitude cuts are adopted taking into account the difference in image depth (mainly g'-band) between the central and the outer regions. For the central 1 deg^2 field, we apply a magnitude cut of $R \leq 24.5$ magnitude. For the outer 1.63 deg^2 area surrounding the central region, we adopt $R \leq 23.5$ magnitude cut. Note that u, g, and R magnitudes are corrected for the galactic extinction (Shim et al. 2006; Fadda et al. 2004).

The colors of star-forming galaxies at $2.8 < z < 3.6$ falls into the selection box (Figure 2). The lines in the upper left of the color-color plot represent the location of model galaxies with constant star formation rate at $z \sim 3$, of various ages and extinction values (see Figure 2 caption). Note that the lines represent galaxies with the solar metallicity, and the metallicity lower than the solar would move the lines to the left.

The color selection criteria can select star-forming galaxies with constant star formation rate at the age of ~ 10 Myr to ~ 2 Gyr. The criteria can also select star-forming galaxies with exponentially decaying star formation rate at the age up to the exponential time scale τ. Regardless of its star formation history, a galaxy younger than ~ 100 Myr falls into the selection box. When there is internal extinction, the limit on
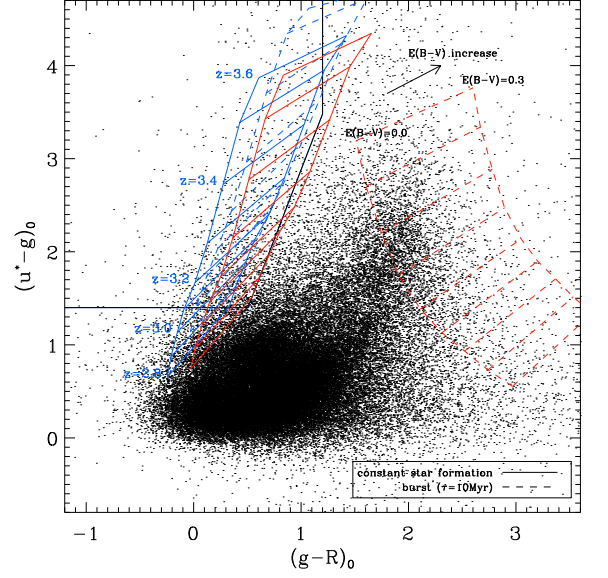

FIG. 2.— The $g-R$ versus u^*-g color-color diagram of galaxies in XFLS. Using the expected tracks of galaxies at the redshift range of $2.8 < z < 3.6$ with different age/star formation history/dust extinction, we identify the boxed region in the upper left as the place where the LBGs reside. The *solid* lines indicate galaxies with constant star formation, and the *dashed* lines indicate galaxies with single-burst star formation history. Different line colors indicate different ages, blue for 50 Myr-old galaxies and red for 1 Gyr-old galaxies. The shifts in x-axis direction represent the amount of dust extinction. Galaxies with constant star formation younger than 2 Gyr can be selected using the specified criteria. Young galaxies that have burst-like star formation history can also be selected, but old galaxies at their passively evolving stages (red, *dashed* line on the right) cannot be selected with this criteria.

age of galaxies that can be selected with the criteria changes. For example, the star-forming galaxies with age less than 500 Myr can be selected if $E(B-V) \lesssim 0.3$. Passively evolving galaxies as old as ~ 1 Gyr at $z \sim 3$, which are growing old after a single burst, cannot be selected by this criteria (red, dashed line on the right in Figure 2).

After selecting u-dropouts from the color-color space, we remove spurious objects through the visual inspection. We find that spurious objects are mostly lying near the edge of the image, or too close to bright stars. On the other hand, we exclude objects that are likely to be a low-redshift interlopers based on either spectroscopic redshifts or photometric redshifts (see SED fitting section on Section 4.1).

Finally as a result, we identify 1088 u-dropouts in our search area (925 objects with $R \leq 24.5$ mag in the central 1 deg^2, and 163 objects with $R \leq 23.5$ mag in the outer 1.63 deg^2). Table 1 shows the result. As mentioned in the above paragraph, the numbers in Table 1 are corrected for possible low-redshift interlopers based on their photometric redshifts or spectroscopic redshifts. At $R > 23$ mag, the number density of u-dropouts of our study is consistent with the LBG surface density from previous studies (e.g., Steidel et al. 1999). At $22.5 < R < 23$, our surface density appears to be about twice higher than those found in Steidel et al.(1999), although 1-σ error bars of the two numbers overlap. On the other hand, our number is about three times lower than those found by Hildebrandt et al. (2005). The possible explanations for the discrepancy are (i) low-redshift interlopers; (ii) the cosmic vari-

TABLE 1
SURFACE DENSITY OF u-BAND DROPOUT OBJECTS

R_{AB} magnitude	N [a]	number density [b] (deg^{-2})	Steidel+99 [c] (deg^{-2})	Hildebrandt+05 [d] (deg^{-2})
22.0–22.5	11	4.18±1.26 (1.72)	⋯	⋯
22.5–23.0	35	13.31±2.25 (4.33)	6.77±3.38	34.2±10.8
23.0–23.5	188	71.48±5.21 (20.6)	71.06±13.54	72±18
23.5–24.0	247	247±15.7 (35.5)	294.4±37.22	234±28.8
24.0–24.5	607	607±24.6 (81.9)	656.50±54.14	540±54
	1088			

[a] u-band dropouts are selected in the effective area of 2.63 deg^2 when $R \leq 23.5$ mag, and 1 deg^2 when $R \leq 24.5$ mag.

[b] The errors are given for the Poisson noise only, and in the parenthesis, the errors considering both the Poisson noise and the galaxy clustering noise ($\sigma^2 = \sigma^2_{Poisson} + \sigma^2_{clustering}$) are given. To calculate the clustering error, we used the approximation formula in Peebles (1975), adopting the amplitude of the angular two-point correlation function of $I_{AB} < 24.5$ LBGs in Foucaud et al.(2003). The value in Foucaud et al.(2003) was consistent with our own derivation within ~ 30 %.

[c] The surface number density of $z \sim 3$ LBGs from Steidel et al.(1999). The errors given here represents the Poisson error. Steidel et al.(1999) used $\mathcal{R}$ filter, which is slightly different from R filter with $\mathcal{R}_{AB} - R_{AB} = -0.11$ (Foucaud et al. 2003).

[d] The surface number density of $z \sim 3$ LBGs (u-dropouts) in CDF-South (Hildebrandt et al. 2005). The areas used in their studies are ~ 900 arcmin^2.

TABLE 2
SUBSETS OF LBG SAMPLE

Group	total	3.6μm	4.5μm	5.8μm	8.0μm	24μm
ver (1) ($R <$24.5)	189	22	21	6	7	4
cent(2) ($R <$24.5)	736	21	20	2	3	2
outer (3) ($R <$23.5)	163	20	18	4	4	6

NOTE. — (1) The IRAC verification field (~ 0.22 deg^2) (2) The central part excluding the verification (i.e., effective area: ~ 0.77 deg^2) (3) The outer ~ 1.63 deg^2 field

ance; and (iii) AGN contribution (see Section 5.1 and Figure 6). Spectroscopic observation of bright LBGs should be able to determine which explanation is right. Our study has an advantage over previous ones in terms of the area coverage (~ 2.63 deg^2), thus the Poisson errors in the number density estimates are significantly reduced.

3.2. Mid-Infrared Detection of LBGs

The infrared fluxes of u-dropout objects are obtained from the published IRAC/MIPS source catalogs when available (Lacy et al. 2005; Fadda et al. 2006). If the object flux is not available, we measured the object flux through empirical PSF fitting, applying aperture correction values from Lacy et al.(2005). To reduce uncertainties in flux measurement, we use only objects whose fluxes exceed 3-σ flux limits in IRAC. The number of u-dropouts detected in each IRAC band is summarized in Table 2. Here, we define LBGs detected over 3-σ limit in 3.6 μm image as an IRAC-detected LBGs (hereafter, IRAC LBGs) since all the objects detected in other IRAC bands are also detected in 3.6 μm.

The number of IRAC LBGs is dependent on the depth of the Spitzer image. For example, the number of detections in Table 2 is relatively small compared to the deeper surveys because of the shallower depth of our survey (e.g., Barmby et al. 2004; Huang et al. 2005). Note that, at the same infrared flux limit, the number of IRAC detections in our study is consistent with the other studies. For example, we find 22 IRAC LBGs above the 3 σ flux limit of 6 μJy (3.6μm) in the FLS verification strip (900 arcmin^2). On the other hand, Huang et al.(2005) have identified 8 LBGs and 3 QSO/AGNs in 3.6 μm image at the same flux limit, over 227 arcmin^2 (see Figure 1 in Huang et al. 2005). If we scale the area coverage, we would expect that we could find ~ 6 objects in 227 arcmin^2 of Huang et

al.(2005). These numbers are relatively consistent with each other. Huang et al.(2005)'s sample includes LBGs as faint as $24.5 < R < 25.5$ while we do not. This R-band difference may cause a slight discrepancy between the two numbers, but the difference is almost negligible for the LBGs bright in the rest-frame NIR wavelengths which also turn out to be massive LBGs. Given the bright rest-frame NIR flux, we find that IRAC LBGs belong to massive, IR-bright end of LBGs (see Section 5.2 for more detail). Our sample is biased against UV-faint LBGs due to the bright R-band magnitude cut, but the above comparison suggests that the bias does not affect our analysis of massive LBGs since they are mostly bright in IRAC wavelengths.

For the MIPS detection, we matched our IRAC LBGs with MIPS 24 μm sources in Fadda et al.(2006). In the verification field, 6 IRAC LBGs found matches in the 24 μm catalog (over 5 σ detection, corresponding to $S_{24} \sim 150\mu$Jy). From the shallower parts of the FLS field, 6 objects are found to be in the 24 μm catalog (5 σ, 300μJy). We call these LBGs detected in 24 μm as "24 μm LBGs" [4]. In total, we have twelve 24 μm LBGs from 1088 u-dropouts in our sample. Similarly to the case of IRAC LBGs, MIPS-detection is dependent on the depth of the image, and the number of 24 μm detections can certainly go up if we had a deeper MIPS image. The 24 μm LBGs are IR-luminous sub-population of $z \sim 3$ IRAC LBGs with $L_{IR} > 10^{12} L_\odot$ (See section 5.3 for more detail).

4. SED FITTING

We have performed SED fitting in order to derive various parameters, especially focusing on the stellar masses of

[4] Among non-IRAC LBGs, 2 objects found their matches in 24 μm images. However, we didn't include them in 24 μm LBG sample since their properties are hard to constrain with limited optical photometry.
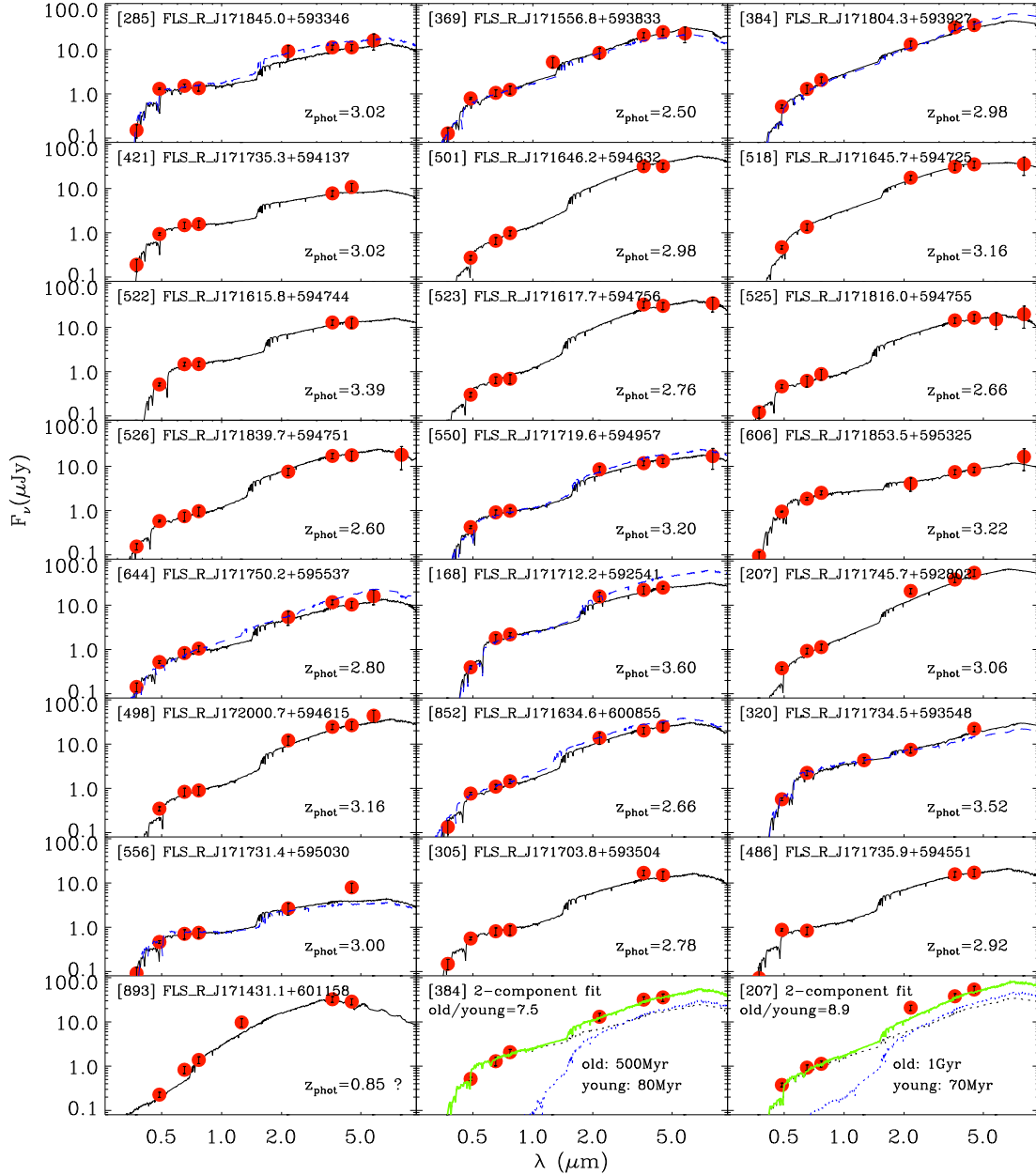
FIG. 3.— The SED fitting results for a representative subset of our LBG sample. The x-axis is the observed wavelength, and the photometric data points are indicated for u, g, R, i, J, K_s, IRAC channel 1, 2, 3, and 4 at 0.374, 0.487, 0.651, 0.768, 1.26, 2.16, 3.6, 4.5, 5.8, and 8.0 μm. The object IDs are drawn from R-band catalogs of Fadda et al.(2004). The *solid* line is the best-fit template using all the photometry data-points. For some objects, a *dashed* line that indicates the best-fit template without MIR data-points is also overplotted.

LBGs. The SED fitting method employs the same methodology as previous studies (e.g., Papovich et al. 2001; Shapley et al. 2001). Various galaxy SED templates were generated using a stellar population synthesis model (Bruzual & Charlot 2003), and fitted to the observed SED. We used all the available photometric data points from u-band to IRAC 8 μm. Note that if we have u, g, and R-band data only, we did not perform the SED fitting since it was very difficult to gain meaningful fit-results from three photometric data points. For optical fluxes, we used MAG_AUTO in SExtractor, while infrared fluxes were measured from the PSF fitting or drawn from the catalog (Lacy et al. 2005) as described in the previous section. In the NIR, the LBG candidates were matched with J- and K_s-band catalogs (MAG_AUTO from SExtractor;

Choi et al. 2007, in preparation) within the matching radius of 1.2″.

For the generation of various galaxy SEDs, we limited our templates to a specific star formation history. The galaxies have the exponentially decaying form of ($\phi(t) \propto exp(-t/\tau)$) star formation with τ=10Myr, 100Myr, 300Myr or a constant star formation rate. In our case, the best-fit SED of almost all the LBGs gives a constant star formation template (cf. Rigopoulou et al. 2006). The metallicity and the initial mass function are fixed to certain values/form. The adopted metallicities are either 0.2 $Z_\odot$ or 1 $Z_\odot$. The IMF was fixed as the Salpeter IMF between 0.1 $M_\odot$ and 100 $M_\odot$. The stellar population was evolved using Padova 1994 stellar evolutionary tracks. The ages of a galaxy, t, was chosen from ~22 possi-
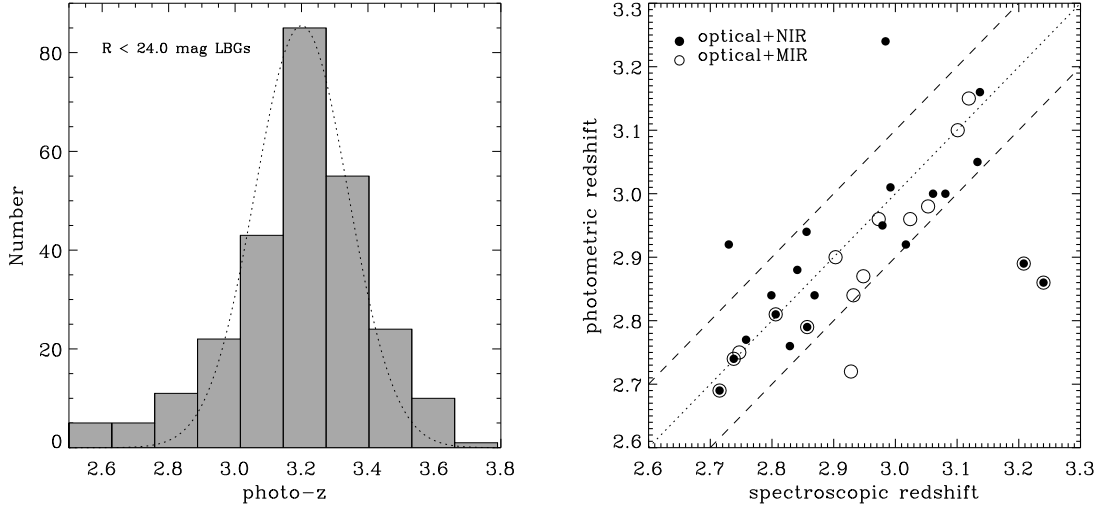
FIG. 4.— *Left*: The photometric redshift distribution of our LBG sample derived from SED fitting. *Dotted* line is an approximation of the distribution as a Gaussian function. Mean redshift $\langle z \rangle$ is ~ 3.2, and the standard deviation of the distribution is ~ 0.14. *Right*: The comparison between spectroscopic redshifts and photometric redshifts of LBGs in the Westphal field (Steidel et al. 2003). Open circles represent 8 micron detected LBGs from Rigopoulou et al. (2006), while filled circles indicate other LBGs with at least one NIR (J, K_s) photometry. Among the 8 micron LBG sample, only 6 objects have NIR photometry (points with both filled and open circles).

ble values between 10 Myr to the age of the universe at the corresponding redshift. The galactic reddening of the generated spectra is following the dust extinction law for starburst galaxy (Calzetti et al. 2000). We also added the flux suppression shortward of Ly α forest due to the intergalactic medium following Madau et al.(1995).

The best-fit parameters - photometric redshift z, extinction parameter $E(B-V)$, stellar mass, age, star formation history and metallicity - are obtained by minimizing the error-weighted χ^2 value expressed as $\chi^2 = \sum_{i,filter} \frac{(f_{obs} - \langle F_\nu \rangle)^2}{\sigma_{obs}^2}$. Note that ages, star formation histories, and metallicities are chosen from discrete values as explained above.

An illustration of SED fitting for some galaxies is presented in Figure 3, including SEDs of possible low-redshift interlopers.

4.1. *Photometric Redshift*

The distribution of photometric redshifts of u-dropouts is presented in Figure 4a. The median redshift of LBGs is $\langle z \rangle \sim 3.2$, and the standard deviation of the photometric redshift distribution of LBGs is ~ 0.14. The u-dropouts are distributed mostly at $2.5 < z < 3.8$, but there is a low redshift tail to the distribution. We consider those having low photometric redshifts to be interlopers.

For example, 5 objects out of the "initial" IRAC LBGs are turned out to have probable redshifts much less than 3. The best-fit SED results for these objects are heavily attenuated, moderately old galaxies at $z \sim 1$ (see the first object in the last row of Figure 3 as an example). Among these, 3 objects were identified to lie at $z = 0.46, 0.96$, and 1.26 in match with the spectroscopic sample of $z \sim 1$ galaxies (Choi et al. 2006). The "possible contaminants" are characterized by red $g-R$ and $R-i$ colors, bright NIR flux (J), and decreasing MIR flux from $3.6\,\mu$m to $8.0\,\mu$m which suggests that $1.6\,\mu$m H$^-$ bump has not redshifted out of $3.6\,\mu$m. For LBG candidates with only g, R, and i detections, low-redshift interlopers are also identified as objects with red $g-R$ and $R-i$ colors. When there are even no i detection, it was difficult to determine which u-dropouts are low-redshift interlopers. However, the non-detection in i-band

suggests that they have blue $g-R$ colors which is indicative of LBGs at $z \sim 3$.

Through these breakdown of the low-redshift interlopers, we removed u-dropouts that have most probable photometric redshifts of $z < 2$. Our investigation shows that the fraction of possible low-redshift interlopers is higher at the brighter R-band magnitude bin. Among u-dropouts, the fraction of possible interlopers with low photometric redshifts is $\sim 25\%$ at the brightest ($22 < R < 22.5$) bin, $\sim 13\%$ at the second brightest ($22.5 < R < 23.0$) bin. For the other bins, the fraction is of order of $\sim 5\%$. Three spectroscopically confirmed low-redshift galaxies mentioned above and galaxies with low photometric redshifts are excluded in Table 1 and in the statistical analysis hereafter. A future spectroscopic study of bright LBGs will be able to determine how reliable the estimates of the number of interlopers are.

In order to check the reliability of our photometric redshift, we tested our method on spectroscopically confirmed LBGs in the extended Westphal-Groth strip (Steidel et al. 2003; hereafter Westphal LBGs). For the photometric data, we used the optical, NIR, and MIR photometry of Westphal LBGs in Shapley et al.(2001) and Rigopoulou et al.(2006). All the LBGs used in this test have at least one photometric data point at wavelength longward of the optical (i.e., NIR or MIR).

Figure 4b shows the comparison of our photometric redshifts versus spectroscopic redshifts. Although there exist a few outliers, in overall the plot shows that the derived photometric redshift is quite reliable to about $\Delta z/z \sim 0.1$, regardless of whether we have NIR or MIR data.

4.2. *Stellar Mass*

Stellar mass is known to be a robust parameter that can be constrained relatively easily compared to other parameters, by being insensitive to the assumed star formation history (e.g., Papovich et al. 2001; Rigopoulou et al. 2006). Other constraints, such as metallicity, are found to affect the derived stellar mass within a factor of 2–5 (Papovich et al. 2001). In addition to that, it has been reported that the inclusion of MIR photometry data points reduces the stellar mass uncertainties by a factor of 1.5–2 (Shapley et al. 2005). Here, we inves-
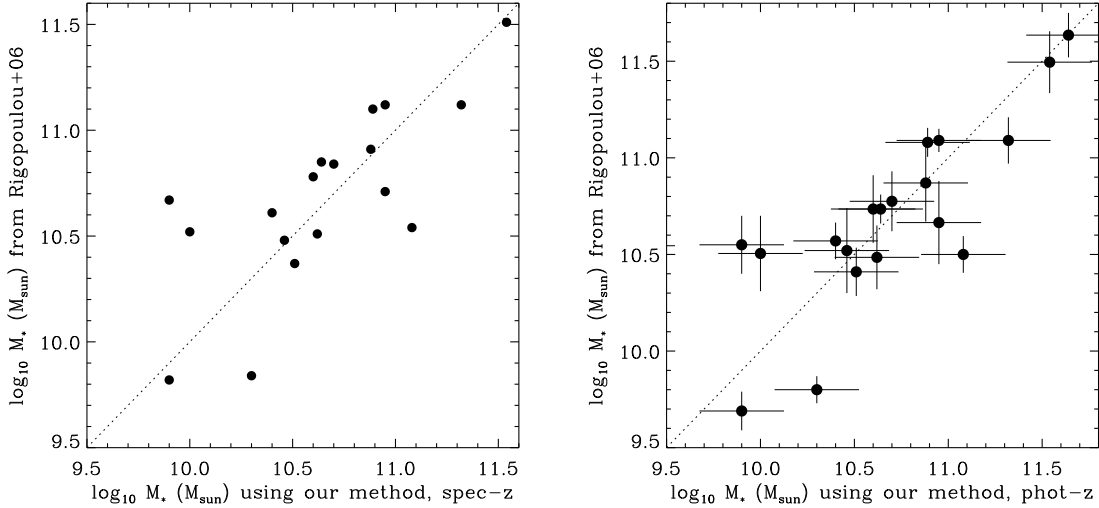
FIG. 5.— *Left*: The comparison of the stellar masses derived using spectroscopic redshifts and our method against that of Rigopoulou et al.(2006). *Right*: The comparison of the stellar masses using photometric redshifts and that of Rigopoulou et al.(2006). The stellar masses estimated by two different methods agree with each other within the errors.

tigate how our stellar masses fare with the values from other methods, and also how much the lack of spectroscopic redshifts influences the stellar mass derivation. Again, we use the Westphal LBGs for this purpose (Rigopoulou et al. 2006).

To inspect the uncertainty arising from photometric redshift, we performed this comparison using spectroscopic redshifts first (Figure 5a). Then, we estimated stellar masses using photometric redshifts instead of spectroscopic redshifts (Figure 5b), and studied how the use of the photometric redshifts affects the result.

Figure 5a shows that our stellar masses derived with spectroscopic redshifts are consistent with those from Rigopoulou et al. (2006) within ≤ 0.2 dex. Therefore, we consider the inherent amount of stellar mass uncertainty due to the fitting method to be ~ 0.2 dex. Figure 5b shows that stellar masses derived with photometric redshifts are within 0.1–0.2 dex from those derived with spectroscopic redshifts. Considering that the uncertainty of stellar masses is dependent on the fitting method by about ~ 0.2 dex, the stellar masses derived with photometric redshifts and spectroscopic redshifts are consistent within the error from the fitting method. Two objects show relatively large discrepant values (objects at around [10.0, 10.5]), but this can be explained with a failure of the fitting since these objects have large χ^2 values. In addition, we have tested two-component fitting for several objects (see last 2 objects in Figure 3) to see how the presence of an underlying old stellar population affects the derived stellar mass. For the two components, we used an old component (500Myr or 1Gyr passively evolving population after single burst) and a young component (constant star forming population younger than 100Myr). The result shows $\sim 20\%$ of difference in the derived stellar masses compared to those derived using a single-component fitting. Since the discrepancy is relatively small, we used single-component fitting only.

5. RESULTS

5.1. *Bright End of the Luminosity Function*

We have constructed the UV luminosity function of our LBGs using the entire sample corrected for interlopers (Table 1). At $2.5 < z < 3.8$ where our LBGs are distributed, the central wavelength of R-band corresponds to 1360Å–1860Å.

Therefore, we converted R-band magnitude to the absolute magnitude with the K-correction consisting of the bandwidth dilation term only, and used it as the UV absolute magnitude. The UV luminosity derived this way samples different rest-frame UV wavelengths at different redshift, but the effect due to this should be less than a few tenths of magnitude.

To derive the luminosity function, we used the $\frac{1}{V_{max}}$ method (Schmidt 1968; Lilly et al. 1995; Im et al. 2002). The number density of LBGs in each magnitude bin is calculated as

$$\phi(M)[mag^{-1}Mpc^{-3}] = \frac{1}{\Delta M} \times \sum \frac{1}{V_{max}}$$

while ΔM is the size of the magnitude bin. The maximum comoving volume, V_{max} is calculated by the equation

$$V_{max} = \int_{max(z_1,z_{min})}^{min(z_2,z_{max})} \frac{dV}{dz} dz$$

where z_1 and z_2 indicate the lower and the upper limit of the redshift distribution of the galaxies. The z_{min}, z_{max} values represent the minimum and maximum redshift where the galaxy can be detected. dV/dz is the differential comoving volume at redshift z.

Our result is consistent with previous results (Steidel et al. 1999) at the magnitude range of $-22.5 < M_{UV} < -21.0$ (Figure 6). At the bright end, there are two noticeable results: (i) the decrease of error-bars, (ii) a clear excess of bright LBGs compared to the expected number from the best-fit Schechter function. First is due to the large area coverage of this study, since the error-bars in Figure 6 represent the Poisson error only. When the galaxy clustering is taken into account, the error bar increases by up to a factor of 2 over the Poisson statistics. Even after the clustering effects are taken into account (Peebles 1975; please refer to the clustering error in Table 1), our error bars are smaller than those of previous studies.

The excess of bright LBGs are quite interesting, although it has been expected from the high surface density of LBGs at the bright R-band magnitude bin (Table 1). The apparent R-band magnitudes of LBGs with $M_{UV} \leq -23.0$ mag are all between $22 \leq R \leq 23$. Until now, few LBGs have been discovered over $M_{UV} = -23.0$ mag, including six "very" bright ($M_{UV} \sim -25.4$ mag) u-dropouts discovered in SDSS DR1
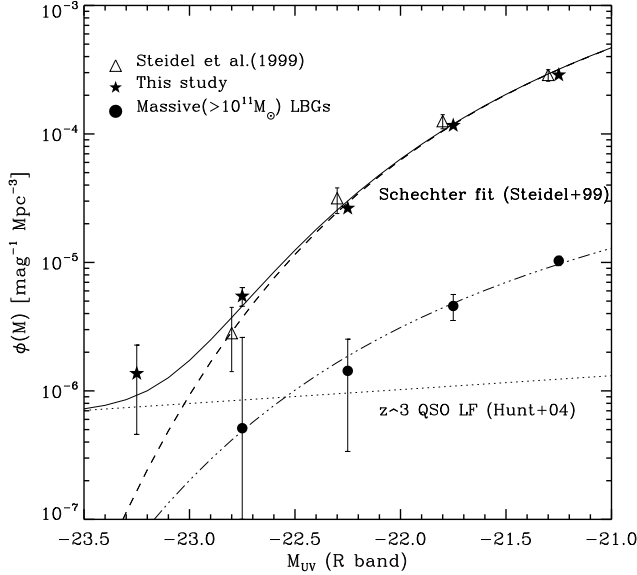
FIG. 6.— The FUV luminosity function of our LBGs, compared with the LF of LBGs and QSOs from Steidel et al.(1999) and Hunt et al.(2004). Note that the size of error-bar of our LF, compared to previous results, has shrunken significantly at bright magnitudes due to the wide area coverage of our survey. *Dashed* line is the best-fit Schechter function for $z \sim 3$ LBGs from Steidel et al.(1999), with $\alpha = -1.6$, $M_* = -21.04$ mag. *Dotted* line is $z \sim 3$ QSO luminosity function from Hunt et al.(2004). *Solid* line is the sum of the $z \sim 3$ LBG luminosity function and the $z \sim 3$ QSO luminosity function. Our data points drawn with stars are consistent with the solid line. At $M_{UV} < -23.0$ mag, the QSO number density exceeds that of LBGs. The significant excess of LBGs at bright end over the Schechter function is most likely to be due to QSOs. The number density of massive ($> 10^{11} M_\odot$) LBGs are overplotted as filled circles. We derived the best-fit parameters for Schechter function to be $\alpha = -1.6$, $M_* = -21.6$ mag (*3-dot-dashed* line).

(~ 1360 deg^2; Bentz et al. 2004). Possible candidates of these bright LBGs are galaxies magnified by gravitational lens (e.g., cB58; Williams & Lewis 1996), quasars, late-type stars, and low-redshift interlopers as we noted in Section 4.1. Among these possibilities, the most probable cause for bright-end excess is QSOs at $z \sim 3$. According to a previous study of $z \sim 3$ QSOs (Hunt et al. 2004), the number density of faint QSOs exceeds that of the galaxies at the magnitude range of $M_{UV} \leq -23.0$ (Figure 6). The comparison of our LBG luminosity function with the QSO luminosity function at $z \sim 3$ suggests that most of the excess above $M_{UV} \leq -23.0$ can be explained by QSO.

Only one of these $M_{UV} \leq -23.0$ mag UV-luminous LBGs are detected in 24 μm image. This may be due to the depth of 24 μm image, and does not constrain the possibility of R-band bright LBGs being AGNs. If AGN-like LBGs are included in stellar mass analysis, the presence of AGNs may boost up the derived stellar masses. Still, the stellar masses of these bright LBGs are $\sim 10^{10} M_\odot$, with the most massive one of $2.6 \times 10^{10} M_\odot$. Therefore, the excess of these "UV bright" LBGs does not affect the analysis of "massive", i.e., $> 10^{11} M_\odot$ LBGs given in this paper.

5.2. *Properties of IRAC LBGs*

In this section, we investigate the properties of 63 IRAC LBGs (detected in IRAC, $S_{3.6\mu m} > 6\mu$Jy in the verification strip, $S_{3.6\mu m} > 12\mu$Jy in the FLS main field). We focus on the stellar masses and dust properties of IRAC LBGs derived through SED fitting.

5.2.1. *M/L ratio in rest-frame NIR*

Among 63 IRAC LBGs, 43 are identified to be more massive than $10^{11} M_\odot$. The bright rest-frame NIR flux of IRAC LBGs suggest that these reside at the most massive end of the whole LBG population, and Figure 7a shows that on average, IRAC LBGs are at the massive end of the mass distribution of LBGs. In Figure 7a, filled circles represent IRAC LBGs, filled triangles represent LBGs detected in NIR but not in IRAC (13), and small dots represent LBGs detected in g, R, and i-bands only (501). The range of the stellar masses of our LBGs is $2 \times 10^9 M_\odot < M_* < 10^{12} M_\odot$. There is no significant correlation between R-band magnitudes and stellar masses. We estimate the uncertainty involved in stellar mass of each LBG to be of a factor of 2–3.

In the local universe, the rest-frame NIR photometry can be a useful stellar mass indicator (e.g., Bell & de Jong 2001). Even for high-redshift LBGs, the same rule applies. For example, Rigopoulou et al.(2006) have found a correlation between LBG stellar mass and the magnitude getting tighter as the wavelength of the band getting longer. In other words, M/L ratio of galaxies derived in the longer wavelength has smaller scatter compared to the value derived in the shorter wavelength. They used LBGs with $M_* \lesssim 10^{11} M_\odot$, and we extend the M/L analysis of LBGs to objects more massive than $10^{11} M_\odot$, using rest-frame NIR wavelength. Since the number of 8 μm detected LBGs is small in our sample, we use 4.5 μm (rest-frame 1.1μm) flux here instead of 8.0 μm flux (rest-frame K-band). Figure 7b shows the 4.5 μm magnitude (the rest-frame J-band at $z \sim 3$) versus stellar mass. Our result shows that even above $10^{11} M_\odot$, there is a good correlation between the rest-frame NIR flux and the stellar mass, while no trend is found between the R-band magnitude and stellar mass (Figure 7a).

Despite the probable consistency of M/L ratio at rest-frame NIR wavelength, Shapley et al.(2005) reported that there is still a scatter of ~ 10 for M/L ratio of star-forming galaxies at $z \sim 2$ when measured in rest-frame 1.4 μm. We also find that there is an order of magnitude spread in M/L ratio at 4.5 μm. The variation in M/L ratio is mainly due to the differences in star formation history. Old galaxies have higher M/L value in NIR, while young galaxies show lower M/L. We examined the M/L ratios of model galaxy templates with different age and star formation history, and found that M/L ratio of 1 Gyr-old galaxy with constant star formation rate is about 12 times smaller than 1Gyr-old galaxy that have been evolved passively after a single burst ($\tau = 10$Myr). Comparing passively evolving population of different age, the M/L ratio of galaxy can be more than twice higher when its age increases from 200 Myr to 1.5 Gyr.

To demonstrate the above point, in Figure 7b, we mark objects with red optical-MIR color of $(R - 3.6\mu m) > 3.5$ which are presumably old galaxies with squares and those with high ongoing star formation ($> 150 M_\odot/yr$) with open diamonds. Here, the star formation rates are derived from UV luminosity, corrected for the dust extinction using $E(B-V)$ obtained with the SED-fitting procedure. The figure shows that actively star-forming galaxies have M/L ratios about 10 times smaller than red galaxies which have much smaller scatter in the M/L. The star formation activity is a major source that provides a spread of a factor of 10 in the mass-to-light relation even at IRAC wavelengths. The correlation coefficient between $M_{4.5\mu m}$ and $logM_*$ is -0.72 for all LBGs in the figure. When LBGs with large SFR ($\geq 150 M_\odot/yr$) are excluded, the correlation coef-
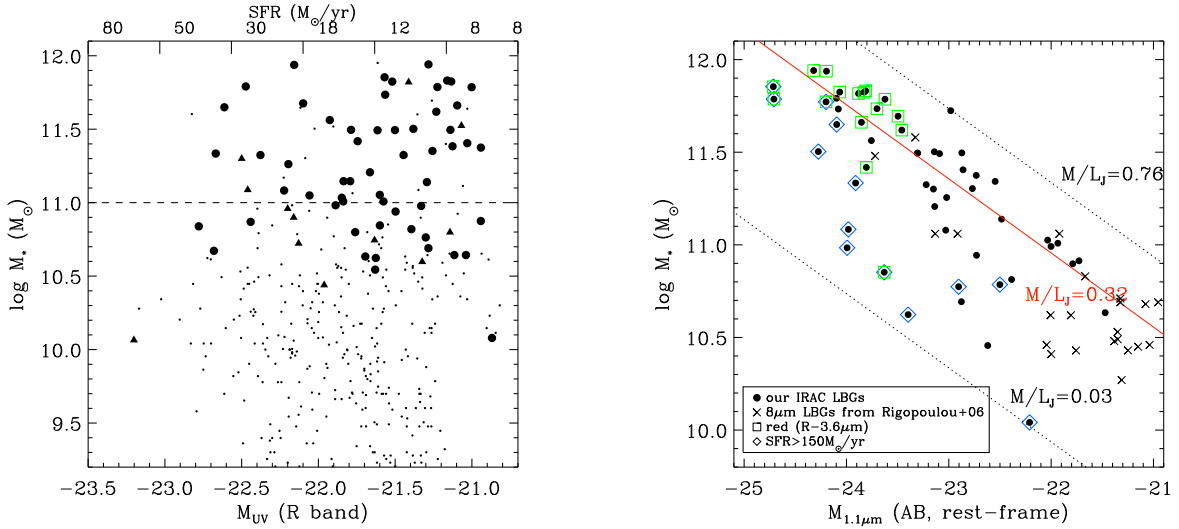
FIG. 7.— The relation between stellar masses and magnitudes (*left*: *R*-band, *right*: 4.5 μm). The plot shows that there is a good correlation between stellar masses and 4.5μm magnitudes (rest-frame *J*-band at $z \sim 3$), while little correlation is shown in stellar masses vs. *R*-band magnitudes (rest-frame UV). (*Left*): Filled circles for IRAC LBGs, filled triangles for NIR-detected LBGs with no detection in IRAC, and small dots for LBGs with optical data points only. (*Right*): Filled circle are IRAC LBGs that have 4.5μm detection. Galaxies with red optical-MIR color (($R-3.6\mu m$) > 3.5) are marked as open squares, and galaxies with ongoing star formation rate larger than 150 $M_\odot/yr$ are specified with open diamonds. The correlation coefficient decreases to $r = -0.85$ from $r = -0.72$ when open diamonds are excluded. The dotted line demonstrates the range of stellar M/L in solar unit. There is a sequence of IRAC LBGs of $M/L_J \sim 0.32$, with an rms error of 0.16 when objects with $M/L_J < 0.1$ are excluded. The stellar masses and 4.5μm magnitudes of 8 micron LBGs from Rigopoulou et al.(2006) are overplotted as crosses. 8 micron LBGs share similar M/L properties with IRAC LBGs.

ficient is −0.85. Also, when objects are restricted to galaxies with red (optical-MIR) colors, we find a tighter correlation between stellar mass and the rest-frame NIR luminosity. Similar effect has also been addressed in Shapley et al.(2005), that $(R-K) > 3.5$ galaxies show tighter correlation in mass-to-light relation among $z \sim 2$ star-forming galaxies.

5.2.2. *Comparison of IRAC LBGs and DRGs*

Previous studies underline the exclusive characteristics among the high-redshift galaxies selected by different criteria. For example, LBGs and DRGs ($(J-Ks) > 2.3$; Franx et al. 2003) are thought to represent blue and small/red and large systems at high redshift (van Dokkum et al. 2006). Little ($< 10\%$) overlap between the two galaxy populations is addressed (Labbé et al. 2005; van Dokkum et al. 2006). Since IRAC LBGs are at the massive end of the LBGs and some of them have red (optical-MIR) color, it is noteworthy to discuss whether these "IRAC LBGs" can also be selected with DRG selection criteria; or at least, whether their mass/color ranges are comparable with those of DRGs.

As for the color, the selection cut for DRGs is $(J-K) > 2.3$, which is sensitive to the underlying old stellar population. There are only small number of IRAC LBGs with both *J*- and K_s-band detection, and their colors are between $0.5 < (J-K_s) < 1.6$. With these, the IRAC LBGs cannot be selected by DRG criteria. However, red (optical-MIR) color cut, for example $(R-3.6\mu m) > 3.5$ to specify galaxies showing tight mass-to-light correlation, is comparable with the color cut of DRGs. Considering the number of $(R-3.6\mu m) > 3.5$ LBGs, we estimate that at least 20% of IRAC LBGs are candidates that could be selected with DRG criteria.

Labbé et al.(2005) suggest that LBGs and DRGs are well-separated in $(I-K_s)$ vs. $(K_s-4.5\mu m)$ diagram in Figure 1 of their paper. LBGs have blue $(I-K_s)$ values ($0 < (I-K_s) < 2$), and DRGs have $(I-K_s) > 2$, redder $(K_s-4.5\mu m)$ color than LBGs. For the IRAC LBGs with K_s-band detection, we find that their color ranges are $1 < (I-K_s) < 4$ and $\langle(K_s-4.5\mu m)\rangle = 0.8$, lying in the space between LBGs and DRGs.

In this respect, IRAC LBGs are close to DRGs – especially in view of stellar masses and ages, inferred from the optical/NIR colors. As for the stellar mass, we show that IRAC LBGs have average M/L ratio of $\langle M/L_J \rangle \sim 0.32$, while the average M/L ratio of DRGs is $\langle M/L_K \rangle \sim 0.33$. Since the rest-frame *J*- and *K*-band fluxes are nearly the same, the M/L ratio of IRAC LBGs is comparable with that of DRGs. It assures the similarity of IRAC LBGs and DRGs.

The fraction of IRAC LBGs in the whole LBG population is $\sim 6\%$, and it can be drawn from the known overlap between LBGs and DRGs, $\sim 10\%$. As is noted in Section 3.2, the fraction is a function of image depth – however, we see that IRAC LBGs represent most of "massive" high-redshift galaxies which could be selected from Lyman break selection criteria.

5.3. *Dust Properties of $z \sim 3$ LBGs*
5.3.1. *24 μm detected IRAC LBGs*

In this subsection, we discuss properties of twelve 24 μm LBGs, which are the IRAC LBGs also detected in the FLS MIPS image (Section 3.2).

First, we investigate the origin of the dust emission, i.e., whether it comes from AGN or starburst. The combination of MIPS 24 μm flux and other IRAC fluxes is known to be a useful indicator to weed out AGNs from star-forming IR-bright galaxies (Egami et al. 2004; Ivison et al. 2004; Yan et al. 2004). Figure 8a shows the ratio of 8 μm flux to 4.5 μm flux ($S_{8.0}/S_{4.5}$) versus the ratio of 24 μm flux to the 8 μm flux ($S_{24}/S_{8.0}$; see Figure 3 of Ivison et al. 2004). Objects that have large $S_{8.0}/S_{4.5}$ and small $S_{24}/S_{8.0}$ are considered to be AGNs in this diagram. Although many objects in our sample have only upper limits in IRAC 4.5 μm, 5.8 μm or 8.0 μm, we examined whether the objects could be classified as AGN or starburst. The result shows that there are 2 possible AGN candidates among our 24 μm LBGs, while the rest can be classified as star-forming galaxies that have MIR colors similar to ILLBG or cold SCUBA sources in Huang et

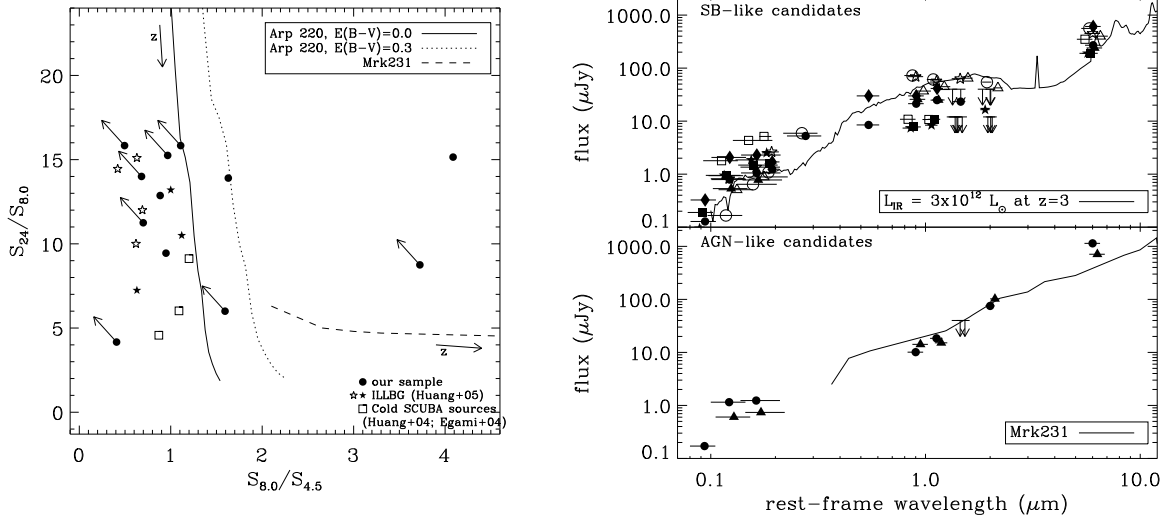FIG. 8.— *Left*: The IR color-color diagram of IRAC LBGs detected in 24 μm. The lines represent tracks of three different spectral templates (*solid* line for ULIRG Arp 220 with no additional reddening;*dotted* line for Arp 220 with $E(B-V) = 0.3$; *dashed* line for dusty AGN Mrk231). At each line, the redshift is increasing downward and to the right. The 24 μm LBGs are plotted as filled circles, with arrows indicating the upper limit value for 8 μm flux. The stars indicate ILLBGs from Huang et al.(2005) that are likely to be starburst galaxies (filled star for spectroscopic sample and open star for photometric sample), and the squares represent cold SCUBA sources (Huang et al. 2004; Egami et al. 2004). Here, starburst galaxies reside in the left part of the plot and the AGNs are located in the bottom-right. *Right*: The spectral energy distribution of 24 μm LBGs. Photometric points of each objects are converted to the rest-frame value using photometric redshift. They are similar to starburst galaxies (*top*), or AGN (*bottom*). Overplotted lines are IR galaxy template with $L_{IR} = 3 \times 10^{12} L_\odot$(*top*, Chary & Elbaz 2001), empirical SED of AGN Mrk 231 (*bottom*).

al. (2005). In a previous discussion, we mentioned that the bright end of the UV luminosity function could be affected by AGNs. Note that the two AGN-type 24 μm LBGs have *R*-band magnitude of 23.7 mag, and 24.3 mag, therefore they are not directly related to the objects consisting of the bright end of the UV-luminosity function.

In Figure 8b, we plot SEDs of the starburst-type and the AGN-type 24 μm LBGs. Solid lines are a SED of a star forming galaxy with $L_{IR} = 3 \times 10^{12} L_\odot$ from Chary & Elbaz (2001) and the SED of AGN Mrk231. The top panel of Figure 8b confirms that most of the 24 μm LBGs have SEDs similar to luminous infrared galaxies with strong starburst activity. The rest-frame NIR part of their SEDs is nearly flat or only moderately increasing toward the longer wavelength, suggesting that the rest-frame NIR fluxes are mostly due to stellar light. The broad PAH emission features at the rest-frame 6–8 μm shift to 24 μm at $z \sim 3$, therefore we interpret 24 μm detection to be due to PAH emissions. On the other hand, the two AGN-type 24 μm LBGs have a strong power-law continuum typical of AGNs (Figure 8b, bottom). One of these AGN-like LBGs is detected in VLA 1.4 GHz with the flux of 0.59 mJy, which suggests that this object is a radio-loud AGN.

In order to derive total infrared luminosities of 24 μm LBGs, we assumeed the SED of M82 ($L_{IR} \sim 3 \times 10^{10} L_\odot$; Telesco & Harper 1980) which is found to resemble SEDs of submm galaxies at high redshift (e.g., Lutz et al. 2005; MenÃl'ndez-Delmestre et al. 2007) The derived infrared luminosities are of order of a few $\times 10^{12} L_\odot$ to $10^{13} L_\odot$ (Table 3), suggesting that the 24 μm LBGs are Ultraluminous Infrared Galaxies.

Alternatively, we tried to estimate L_{IR} of 24 μm LBGs using infrared SED templates of Chary & Elbaz (2001), in which the MIR flux correlates with L_{IR} as $L_{IR} \propto L_{6.7\mu m}^{1.62}$. With such a method, we obtain unreasonably high values of $L_{IR} \sim 10^{14} - 10^{15} L_\odot$ for 24μm LBGs. If 24 μm LBGs were really as bright as $L_{IR} \simeq 10^{14} - 10^{15} L_\odot$, their 850 μm flux would be well above 10 mJy, and they shoud be detectable with submm

observations. However, the existing submm data with a partial coverage of FLS show no detection of 24 μm LBGs providing the flux limit of < 5 mJy (Sawicki & Webb 2005; Kim et al. 2007, in preparation). Therefore, we conclude that cautions are needed when deriving L_{IR} of $z \sim 3$ objects using the correlation between MIR flux and IR flux such as those found in Chary & Elbaz (2001).

We now investigate the dust properties of 24 μm LBGs by comparing SFRs derived from UV luminosity (corrected for dust extinction) and also from IR luminosity. When deriving SFRs from UV luminosity, two methods are used to correct for the dust extinction. One method uses the UV slope β defined as $f_\lambda \propto \lambda^\beta$ at 1500–2800Å (Meurer, Heckman, & Calzetti 1999). Since there are no spectroscopic data for our LBG sample, we measured β from the model spectral template which is found to be the best-fit model using optical (u, g, R and i) photometry only. The other method uses the $E(B-V)$ value derived from the SED-fitting and a known correlation between the UV extinction and $E(B-V)$ ($A_{1600} = 4.39E_g(B-V)$; Calzetti et al. 2000). Here, our $E(B-V)$ derived from stellar continuum is related with nebular line-derived $E_g(B-V)$ as $E_s(B-V) = 0.44E_g(B-V)$ (When we use $E(B-V)$ value, we mean $E_s(B-V)$ hereafter). The conversion formula from luminosity to star formation rates are taken from Kennicutt (1998):

$$SFR_{IR}(M_\odot/yr) = 1.71 \times 10^{-10} L_{IR}(L_\odot)$$
$$SFR_{UV}(M_\odot/yr) = 1.4 \times 10^{-28} L_{UV}(ergs/s/Hz)$$

The result is presented in Table 3 and Figure 9. As is shown in the Table 3, the UV-derived SFRs from two methods are consistent with each other, within a factor of 2 in most cases. Between the extinction-corrected UV-derived SFRs and IR-derived SFR, Figure 9 shows that these quantities are consistent with each other within a factor of a few, and with the median ratios of ~ 2 when $SFR_{IR} \lesssim 800 M_\odot/yr$ or $L_{IR} < 5 \times 10^{12} L_\odot$. Note that we ignore two AGN-type objects in this comparison. However, for galaxies with $L_{IR} >$

TABLE 3
COMPARISON OF UV-DERIVED SFR AND IR-DERIVED SFR

object ID	24μm flux (mJy)	UV SFR ($M_\odot/yr$)	UV SFR$_c$ ($M_\odot/yr$)	IR SFR ($M_\odot/yr$)	IR luminosity ($L_\odot$)	$E(B-V)$	A$_{1600}$ (mag)	comment
(1)	(2)	(3)	(4)	(5)	(6)	(7)	(8)	(9)
c[320] FLS_R_J171734.5+593548	0.14 ± 0.05	51.7	424.3 (1413.3)	454.9	2.66×10^{12}	0.36	3.59	$\cdots$
c[369] FLS_R_J171556.8+593833	0.27 ± 0.05	23.8	146.2 (163.9)	877.2	5.13×10^{12}	0.21	2.10	$\cdots$
c[421] FLS_R_J171735.3+594137	0.19 ± 0.05	35.7	107.1 (204.8)	617.3	3.61×10^{12}	0.19	1.90	$\cdots$
c[583] FLS_R_J171430.7+595213	0.24 ± 0.05	16.9	383.4 (242.4)	779.8	4.56×10^{12}	0.29	2.89	$\cdots$
c[606] FLS_R_J171853.5+595325	0.19 ± 0.05	47.6	469.1 (473.6)	617.3	3.61×10^{12}	0.25	2.49	$\cdots$
c[678] FLS_R_J171418.8+595722	0.56 ± 0.05	15.9	955.4 (2723.5)	1812.6	1.06×10^{13}	0.56	5.59	$\cdots$
o[035] FLS_R_J171412.0+591716	0.61 ± 0.05	51.5	204.5 (269.3)	1983.6	1.16×10^{13}	0.18	1.80	?
o[217] FLS_R_J171642.9+585733	0.35 ± 0.05	117.8	200.9 (155.2)	1137.2	6.65×10^{12}	0.03	0.30	?
o[275] FLS_R_J171816.7+584813	0.40 ± 0.06	16.8	620.8 (317.6)	1299.6	7.60×10^{12}	0.32	3.19	$\cdots$
o[306] FLS_R_J172045.2+585221	1.14 ± 0.06	28.2	35.6 (70.8)	3710.7	2.17×10^{13}	0.10	1.00	AGN?[a]
o[429] FLS_R_J172202.1+585414	0.45 ± 0.05	30.9	418.7 (405.7)	1462.1	8.55×10^{12}	0.28	2.79	$\cdots$
o[504] FLS_R_J171618.4+602620	0.71 ± 0.06	15.0	38.6 (23.8)	2308.5	1.35×10^{13}	0.05	0.50	AGN?

NOTE. — (1) ID of the object (drawn from R-band catalogs of Fadda et al.(2004)); (2) 24 μm flux in mJy; (3) uncorrected UV-derived SFR; (4) corrected UV-derived SFR using UV slope β or $E(B-V)$ (see Section 5.3.1 for more detail); (5) IR-derived SFR; (6) IR luminosity using 24 μm flux; (7) $E(B-V)$ derived during the SED fitting process. According to Calzetti et al.(2000), $E_s(B-V) = 0.44E_g(B-V)$, while $A_{1600} = 4.39E_g(B-V)$ for $E_g(B-V)$ derived using nebular gas emission lines; (8) A_{1600} estimated from $E(B-V)$; (9) comments for the objects. Objects marked as "AGN?" are suspicious to be AGNs due to their SED shapes in MIR (see Figure 8 in Section 5.3.1). Objects with "?" mark (o[035], o[217]) are objects with a large discrepancy between UV-derived SFR and IR-derived SFR, thus are suspected to be AGN-dominated.

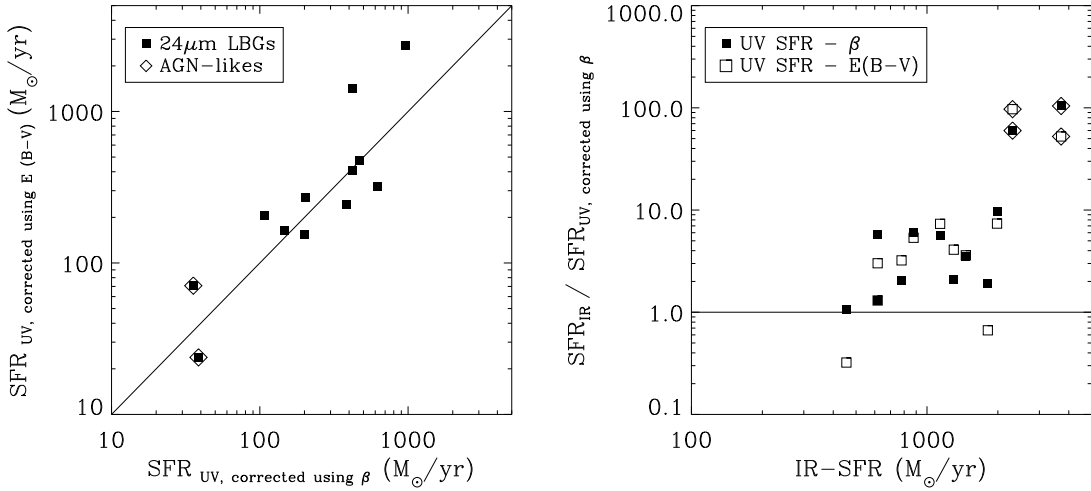[a]This object is detected in VLA 1.4 GHz image, with the flux of 0.59 mJy.

FIG. 9.— *Left*: The comparison between two different extinction correction method to UV-derived SFR. Both method, using UV-slope β or $E(B-V)$ are consistent within a factor of ~ 2. *Right*: The comparison between IR-derived SFR and extinction-corrected SFR. When IR-SFR is below $\sim 800 M_\odot/yr$, extinction-corrected UV-SFR is quite consistent with IR-SFR.

$5 \times 10^{12} L_\odot$ or $SFR_{IR} \gtrsim 800 M_\odot/yr$, we find that extinction-corrected SFR_{UV}s from the both β-correction and the $E(B-V)$ methods are either systematically lower than SFR_{IR} by a factor of a few or have large scatter with respect to SFR_{IR}. If the SFR_{IR} values represent the true star formation rates, this result suggests that the extinction correction at UV tend to be underestimated when $L_{IR} > 5 \times 10^{12} L_\odot$, consistent with the previous findings where it has been found that the UV-slope method appears to systematically underestimate the extinction correction in UV for the most IR luminous galaxies (Papovich et al. 2006; Reddy et al. 2006).

Table 3 shows that the dust-free SFR of LBGs using 24 μm flux is of order of a few hundred to a few thousand $M_\odot/yr$. Assuming that IR luminosity represents the total star forming activity, we derive the extinction correction at 1600Å to be $A_{1600} = 2$–4.5 mag for 24 μm LBGs, by comparing the SFR_{IR} and $SFR_{UV,uncorrected}$. Previous works have found that the

LBGs at $z \sim 3$ have a median extinction value of $\langle A_{1600} \rangle = 1.0$ mag, distributed over $A_{1600} = 0$–4 mag (Adelberger & Steidel 2000). Comparing the extinction values of 24 μm LBGs with the above values, we conclude that 24 μm LBGs are the dustiest population among LBGs.

We also derived A_{1600} from $E(B-V)$. Since we use $E(B-V)$ to correct for the dust extinction of UV luminosity of LBGs in the following analysis, we mention here how reliable the extinction correction using $E(B-V)$ would be. Mostly, there are ~ 2 mag scatter in A_{1600}. First, the comparison between SFR_{IR} and SFR_{UV} suggest that the extinction correction using $E(B-V)$ is reasonably accurate to a factor of ~ 2. Additional uncertainty exists in the relation between A_{1600} and $E(B-V)$ observationally (Calzetti et al. 2000) and theoretically (Witt & Gordon 2000). Calzetti et al.(2000) mention that the linear relation between $E(B-V)$ and A_{1600} represents the lowest envelope of the relation, suggesting the derived A_{1600} might
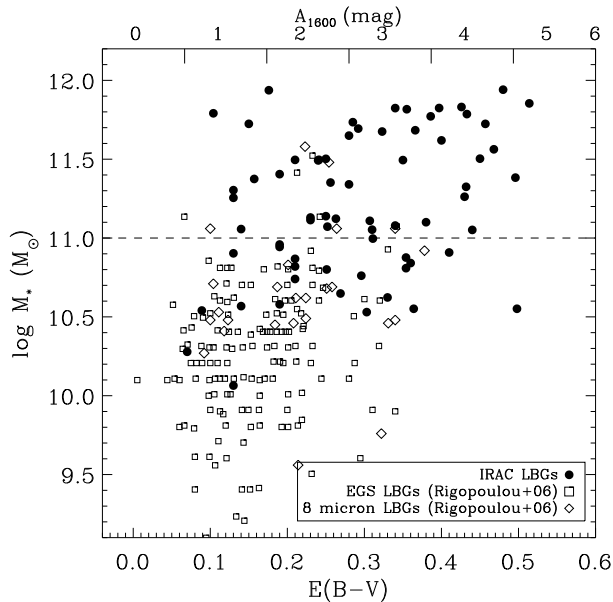
FIG. 10.— The $E(B-V)$ versus the stellar mass. Also, overplotted on the figure are the data points from Rigopoulou et al.(2006). The median value of dust extinction in IRAC LBGs is $\langle E(B-V)\rangle = 0.29$. On average, there is a correlation between dust extinction and stellar mass with a correlation coefficient $r = 0.51$.

FIG. 11.— *Left* is an example of 24 μm postage image of IRAC LBG that is not detected in MIPS 24 μm image. We also present the median-stacked images of 20 IRAC LBGs without 24 μm detection in the verification strip (*middle*), and 49 IRAC LBGs without 24 μm detection in the main field (*right*). The size of each image is $40'' \times 40''$. The stacked image shows a clear signal over 8 σ.

underestimate the dust extinction by a factor of a few.

5.3.2. *Dust property vs. stellar mass*

In Figure 10, we show a plot of dust extinction $E(B-V)$ versus stellar mass. When our massive ($> 10^{11} M_\odot$) LBGs are plotted together with less massive LBGs from Rigopoulou et al.(2006), there is a weak, but positive correlation between $log M_*$ and $E(B-V)$ with the correlation coefficient of $r = 0.51$. Thus, Figure 10 suggests that dustier LBGs tend to be more massive. It has been argued that LBGs with intrinsically higher bolometric luminosity (UV+IR) are more massive (Reddy et al. 2006; $1.5 < z < 2.6$ optically selected LBGs). Large amount of dust in LBG implies high infrared luminosity that leads to high bolometric luminosity, therefore our result is consistent with previous results.

The median value for the dust extinction in IRAC LBGs is $\langle E(B-V)\rangle \simeq 0.29$. This is larger than $\langle E(B-V)\rangle \simeq 0.15-0.20$ of all LBG population (Adelberger & Steidel, 2000) and similar to ILLBGs of $\langle E(B-V)\rangle = 0.354$ (Rigopoulou et al. 2006). We already mentioned in Section 5.3.1 that the mean value for dust extinction is $E(B-V) = 0.28$ for 24μm LBGs. IRAC LBGs and 24μm LBGs share the same range of dust-extinction, while the infrared luminosities of 24μm LBGs are higher than those of IRAC LBGs. By stacking the 24 μm images of LBGs with no individual detection in 24 μm image, we see that the average IR luminosities of IRAC LBGs are slightly lower, but close to those of 24μm LBGs within a factor of a few (presented in Section 5.3.3 in more detail).

5.3.3. *Average infrared luminosity of LBGs*

24 μm-detected LBGs are probably the most infrared-luminous galaxies among all LBGs, with the total infrared luminosity of $\gtrsim$ a few $\times 10^{12} L_\odot$. Since the majority of LBGs are not detected in 24 μm, we examined their IR properties by stacking MIPS 24 μm images.

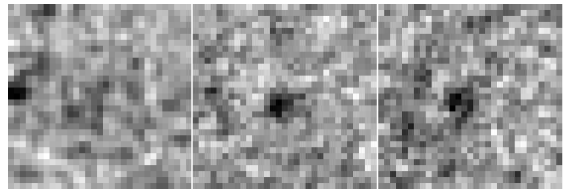First, we examined IR properties of IRAC LBGs. We stacked 24 μm images of 20 IRAC LBGs in the MIPS FLS

verification strip and 49 IRAC LBGs in the main field, both without 24 μm detection (Figure 11). The stacked images show a clear existence of emission in 24 μm. When measured upon the stacked image, the signal to noise ratios are ~ 8 in both the verification and the main fields. The average fluxes of these LBGs, therefore, are 60.4 μJy for 24 μm-undetected IRAC LBGs in the verification strip, and 70.3 μJy for 24 μm-undetected IRAC LBGs in the main field. Converting the expected 24 μm flux to the total infrared luminosity assuming M82 SED, we find that the expected IR luminosity of 24 μm undetected IRAC LBGs is about $\sim 1.1 \times 10^{12} L_\odot$ in the verification strip, and $\sim 1.3 \times 10^{12} L_\odot$ in the main field. The corresponding star formation rate is $180-220 M_\odot/yr$. The estimated 24 μm flux of 60.4–70.3μJy for IRAC LBGs is comparable with the 60 μJy cut for ILLBGs defined in Huang et al.(2005), who suggest the ILLBGs occupy 5% of the total LBGs. The fraction of our IRAC LBGs (63) in the whole LBGs (1088) is similar with their value.

With the same stacking method, we also estimated the average infrared flux of the LBGs not detected in IRAC. The 24 μm images of 300 LBGs in the MIPS verification field with no IRAC detection were stacked, showing a marginal detection of $S/N \sim 3$ or the average flux of 6 μJy. The estimated infrared luminosity of these LBGs is of order of $1.1 \times 10^{11} L_\odot$, or the star formation rate of $19 M_\odot/yr$ according to the conversion relation. This value is consistent with the SFR, $10-100 M_\odot/yr$, of typical LBGs as mentioned in the Introduction. At this relatively low infrared luminosity range, the result from Chary & Elbaz template fitting is not much different from the M82 scaling method; the result is $\langle L_{IR}\rangle = 1.4 \times 10^{11} L_\odot$, the star formation rate of $24 M_\odot/yr$.

5.4. *Implication for Galaxy Formation*

5.4.1. *Number density of massive LBGs*

The number density of massive galaxies at high redshift can show the straightforward evidence of early formation of massive systems. In Figure 12, we plot the number density of massive ($M > 10^{11} M_\odot$) LBGs in filled circle, and compare the value with other observational results (Drory et al. 2005; Saracco et al. 2004; Rigopoulou et al. 2006; McLure et al. 2006) and the predictions from several hierarchical galaxy formation models such as semi-analytic models of Baugh et al.(2003; dotted line), Bower et al.(2006; dashed line), and the hydrodynamic simulation of Nagamine et al.(2005; large solid rectangle). Note that the more recent models (Bower et al. 2006) overcome shortcomings of the earlier model of underestimating the number density of massive galaxies at high redshift (e.g., Baugh et al. 2003), and are successfully predicting the observational constraints at $z \sim 2$.

We find that the number density of our LBGs with mass greater than $10^{11} M_\odot$ is $\Phi = (1.05 \pm 0.15) \times 10^{-5} Mpc^{-3}$. Our
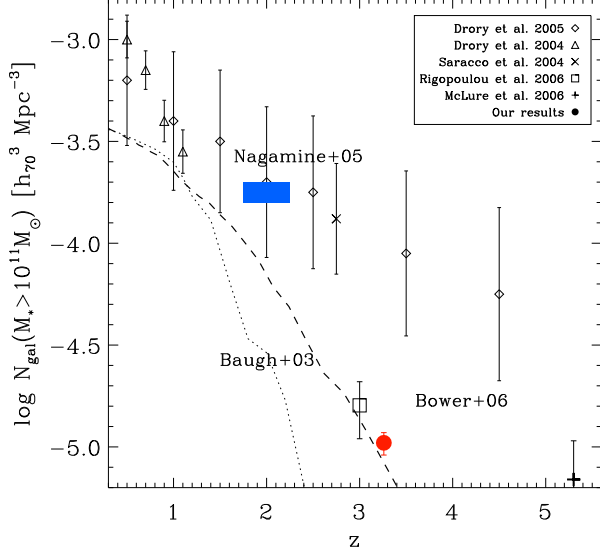
taneous star formation rate using the UV luminosity function presented in Section 5.1, and correcting it for the dust extinction. The FUV luminosity density is derived by integrating the luminosity function over the magnitude interval of the survey,

$$L_{FUV} = \int_{M_{min}}^{M_{max}} L(M)\Phi(M)dM$$

while M_{min} and M_{max} indicate the minimum and maximum absolute FUV magnitudes.

The estimated luminosity density is then converted to the star formation rate density using the conversion formula from Kennicutt (1998) assuming the Salpeter IMF. For the whole LBGs, for which we have an observational constraint on the faint-end slope of UV luminosity function from studies extending to the fainter limits, we get the star formation rate density value (before dust extinction correction) of $\rho_* = 4.0 \times 10^{-2} M_\odot\, yr/Mpc^3$ by using $M_{min} = -\infty$ and $M_{max} = -10$. For the star formation rate density of massive ($> 10^{11} M_\odot$) LBGs, we get a conservative estimate of $\rho_* = 2.3 \times 10^{-4} M_\odot/yr/Mpc^3$ by adopting $M_{min} = -23.5$ and $M_{max} = -21.0$ of our survey limit, since the faint-end slope of UV luminosity function of massive LBGs is not well constrained.

Correction for the dust extinction is done as the followings. According to the discussion in Section 5.3.1, the extinction parameter $E(B-V)$ is a reasonably accurate measure of the dust extinction, except for IR-bright objects with very high star formation rate. For the SFR density from whole LBGs, we adopt the average dust extinction of $\langle E(B-V)\rangle = 0.15$ (Adelberger & Steidel 2000). This average $E(B-V)$ value increases the derived SFR density by a factor of ~ 3.94 (Calzetti et al. 2000; $A(1600\text{Å}) = 4.39E(B-V)$), therefore the extinction-corrected SFR density of the whole LBGs at $z \sim 3$ is $\rho_* = 1.6 \times 10^{-1} M_\odot/yr/Mpc^3$. For the massive LBGs, we use the median $E(B-V)$ value of massive LBGs, $\langle E(B-V)\rangle = 0.29$ (Figure 10), or an extinction correction factor of 14.3. Therefore, the corrected SFR density of massive LBGs is $\rho_* = 3.3 \times 10^{-3} M_\odot/yr/Mpc^3$. As discussed in section 5.3.1, the uncertainty in the extinction correction factor for 24 μm LBGs is about a factor of 2 to 3, but could be larger than that for ULIRG-type objects. We adopt the error bar of a factor of a few as a rough estimate of the SFRD uncertainty.

The star formation rate density value of $\rho_* = 3.3 \times 10^{-3} M_\odot/yr/Mpc^3$ can be considered as a lower limit, since the above calculation do not include the contribution from massive LBGs with $M_{UV} > -21$. The inclusion of the population fainter than our survey limit into the calculation requires an assumption on the faint-end slope of the UV luminosity function. If we adopt a fiducial value of $\alpha = -1.6$ as the faint end slope, we get the star formation rate density of $1.6 \times 10^{-2} M_\odot/yr/Mpc^3$ by adopting $M_{max} = -10$. This is likely to be an upper limit of the star formation rate of massive galaxies, uncertain at a factor of roughly a few. Also, note that the derived SFR would decrease by a factor of ~ 0.25 dex if we adopt the Chabrier IMF (Chabrier 2003) instead of the Salpeter IMF (Dahlen et al. 2007).

Figure 13 shows the SFR density of the LBGs compared to those of galaxies at different redshifts from other works. Various SFR densities in the figure are based on the UV luminosity, although sample selection methods are different. What is interesting in the figure is the contribution of massive galaxies to the total star formation rate density from $z < 2$ (Juneau et al. 2005) and $z \sim 3$ (our result). A direct comparison of our result versus Juneau et al. (2005) is possi-

FIG. 12.— The number density of galaxies with stellar masses $> 10^{11} M_\odot$ as a function of redshift. The red filled circle shows our result for massive LBGs, which is quite comparable with the result of massive LBGs at the similar redshift range by Rigopoulou et al.(2006). Data points from other observations are plotted with different symbols, and the prediction from recent semi-analytic and hydrodynamic models of galaxy formation are overplotted (*dotted* line from Baugh et al. 2003; *dashed* line for Bower et al. 2006; blue filled rectangle from Nagamine et al. 2005).

value is consistent with the value presented in Rigopoulou et al. (2006), who have performed a similar study for LBGs over a smaller area. If we adopt $\sim 20\%$ as the fraction of LBGs among massive galaxies (van Dokkum et al. 2006), the estimated number density of all massive galaxies would increase to $\Phi = (5.25 \pm 0.75) \times 10^{-5} Mpc^{-3}$, consistent with those from NIR-selected sample of Drory et al.(2005). QSO contamination at optically bright LBGs is not likely to affect the number density of massive LBGs since they comprise a small fraction of massive LBGs.

Comparison of our result with the model predictions in Figure 12 shows that the most up-to-date semi-analytic model (e.g., Bower et al. 2006) still underpredicts the number density of massive galaxies, although the discrepancy between the model and the observational constraints is now much reduced. Our result for the number density has uncertainty of a factor of a few, due to the Poisson errors and the small fraction that UV-selected galaxies comprise for the entire massive population. However, considering that the comparison is made for objects at the very massive end of the mass function, the discrepancy could be narrowed without too much difficulty with a slight tweaking of model parameters, or by improving observational constraints with a better number statistics and measurements.

5.4.2. *Contribution of massive LBGs to the total SFR density*

In the downsizing scenario of galaxy formation, the star formation activity occurs early in massive galaxies, and late in less massive galaxies. Therefore, such a model predicts that the relative contribution of the star formation activity from galaxies with different masses should evolve as a function of redshift, with the star formation occurring more in massive galaxies at the higher redshift.

In order to examine the contribution of massive LBGs to the total star formation rate at $z \sim 3$, we calculated the instan-
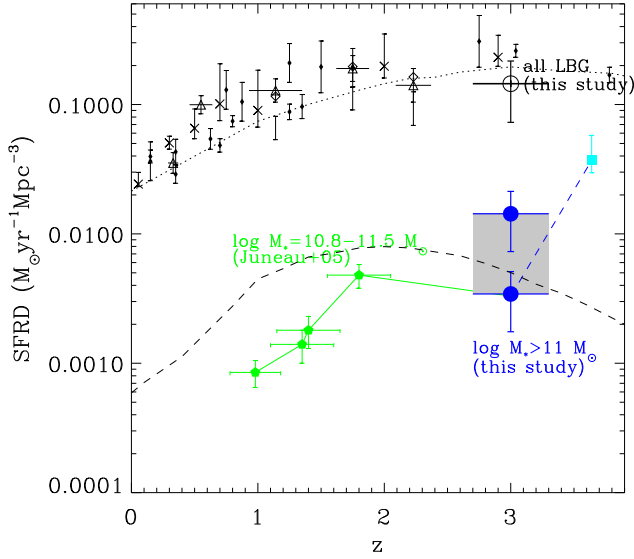
FIG. 13.— The star formation rate density derived from LBGs in FLS. The open/filled circle indicates the star formation rate density from whole/massive ($> 10^{11}M_\odot$) LBGs. The points are corrected for dust extinction, using average $E(B-V)$ value (~ 4 and ~ 14 for whole/massive LBGs). Considering the contribution from LBGs below R-band magnitude limit of our study, the estimated star formation rate density from massive LBGs resides in the shaded box. Green filled pentagons are the SFR density from galaxies whose stellar masses are $10^{10.8}M_\odot < M_* < 10^{11.5}M_\odot$, drawn from Juneau et al.(2005). Other symbols indicate the total SFR density at the corresponding redshift (*open triangle/diamond*: Dahlen et al. 2007; *crosses*: Schiminovich et al. 2006; *filled diamond*: Hopkins 2004). Cyan filled square is the estimate of the SFR density at $z = 3.6$ using nearby massive SDSS galaxies (Panter et al. 2006). Overplotted *dotted/dashed* lines are the prediction of the evolution of star formation rate density from all/massive galaxies along redshift (Bower et al. 2006).

ble, since galaxies contributing to the most SFR in the K-band selected sample of Juneau et al.(2005) are star-forming galaxies which also appear to be UV-bright (cf. Burgarella et al. 2006). Despite the slight difference in stellar mass range ($10^{10.8}M_\odot < M_* < 10^{11.5}M_\odot$ in Juneau et al. 2005; $M_* > 10^{11}M_\odot$ in our study), our result is consistent with the view that the contribution of massive galaxies to the total SFR has steadily decreased from $z \sim 3$ to the present, and possibly providing toward an even higher contribution at $z \sim 3.6$ as suggested by Panter et al. (2006). On the other hand, a large uncertainty in our data point does not exclude a possible peak SFR activity for massive galaxies at $z \sim 2$ as predicted in a semi-analytical model of Bower et al. (2006; dashed line). Clearly, a better constraint is needed by extending the study to the fainter limit, and placing more constraints on the extinction within high-redshift galaxies.

Our SFR density at $z \sim 3$ does not include the contribution from the UV-faint population that cannot be selected using Lyman break technique, such as DRGs or submm galaxies. The contribution of massive galaxies to the star formation at $z = 3$ can go up even more if we include the contribution from the galaxies that are heavily extinguished by dust. The number density of submm galaxies is very small, $8.9 \times 10^{-6} Mpc^{-3}$ at $1.8 < z < 3.6$ (Tecza et al. 2004). Although there might be an overlap of order of 50% between LBGs and submm galaxies (e.g., Chapman et al. 2005), the submm galaxies can have star formation rates as large as 1000 $M_\odot/yr$, therefore their SFR density can be almost comparable to the SFR density of massive LBGs. The contribution of DRGs is rather difficult

to estimate. Förster-Schreiber et al.(2004) suggested that the median value of the star formation rate for DRGs in HDF-S is 120 $M_\odot/yr$, and their number density is about an order of magnitude greater than submm galaxies (van Dokkum et al. 2006). From the above fact, one might argue that the SFR density of DRG is comparable to that of massive LBGs, but such an argument is not valid since these two populations overlap with each other as mentioned in Section 5.2.2.

In any case, our result suggests that the star formation activity in massive galaxies is a dominant process at $z = 3$ compared to the universe at $z < 1$, supporting the downsizing picture of the galaxy formation.

6. CONCLUSION

We have selected and studied LBGs at $z \sim 3$ in the *Spitzer* First Look Survey area, using the multi-wavelength datasets consisting of deep u, g, R, and i', J, K_s-band and the *Spitzer* IRAC and MIPS images. In total, we have found 1088 LBGs with $R = 22.0$–24.5 mag over the ~ 2.63 deg^2 area. The wide area coverage enables us to select a large number of bright LBGs with MIR fluxes which are important for studying various properties of rare, massive LBGs.

Particularly, we concentrated on the properties of LBGs detected in IRAC 3.6μm over 3σ (6μJy in verification strip, 12μJy in main field). These "IRAC LBGs" are on average massive/old/infrared sub-population of whole LBGs. Nearly $\sim 70\%$ of IRAC LBGs are more massive than $10^{11}M_\odot$. IRAC LBGs with the largest stellar mass have the reddest (optical-MIR) color, which is indicative of old stellar population. M/L ratio of the galaxies dominated by old stellar population is constant with little scatter. On the other hand, IRAC LBGs with large ongoing star formation increase the scatter in M/L.

Among these IRAC LBGs, 12 LBGs were detected in 24 μm image. The infrared luminosity of the LBGs with individual 24 μm detection suggests a high star formation rate of $\sim 1000M_\odot/yr$ occurring in these systems. The $E(B-V)$ of LBGs, indicating the amount of dust extinction within the uncertainty of a factor of a few, has weak but existing correlation with the stellar mass. Dustier LBGs are more massive, and this again ensures we see the massive/infrared end of LBG population in the IRAC LBGs.

With the photometric redshifts of the LBGs, the rest-frame UV luminosity function is constructed. The derived luminosity function is consistent with previous studies, but with a much improved number statistics. We also construct the UV luminosity function of massive LBGs ($> 10^{11}M_\odot$), from which we estimate the SFR density in massive systems at high redshift. The star formation rate density from all LBGs at $z \sim 3$, calculated in the survey magnitude interval, is $\rho_* = 1.6 \times 10^{-1}M_\odot/yr/Mpc^3$, while the star formation rate density from massive LBGs is $\rho_* = 3.3 \times 10^{-3} \sim 1.6 \times 10^{-2}M_\odot/yr/Mpc^3$. The contribution of the massive systems to the global star formation at $z \sim 3$ is significantly large compared to the case of lower redshifts. This finding suggests that the shift of star formation activity from massive systems to the smaller systems as the universe ages, interpreted as known "downsizing" of the galaxy formation and evolution.

REFERENCES

Adelberger, K. L. & Steidel, C. C. 2000, ApJ, 544, 218

Barmby, P. et al. 2004, ApJS, 154, 97

Baugh, C. M., Benson, A. J., Cole, S., Frenk, C. S., & Lacey, C. 2003, The Mass of Galaxies at Low and High Redshift Proceedings of the ESO workshop

Bell, E. F. & de Jong, R. S. 2001, ApJ, 550, 212

Bentz, M. C., Osmer, P. S., & Weinberg, D. H. 2004, ApJL, 600, 19

Bertin, E. & Arnouts, S. 1996, A&AS, 117, 393

Bouwens, R. J. et al. 2004, ApJ, 616, 79

Bower, R. G., Benson, A. J., Malbon, R., Helly, J. C., Frenk, C. S., Baugh, C. M., Cole, S., & Lacey, C. G. 2006, MNRAS, 370, 645

Bruzual, G. & Charlot, S. 2003, MNRAS, 344, 1000

Burgarella, D. et al. 2006, A&A, 450, 69

Calzetti, D., Armus, L., Bohlin, R. C., Kinney, A. L., Koornneef, J., Storchi-Bergmann, T. 2000, ApJ, 533, 682

Chabrier, G. 2003, PASP, 115, 763

Chapman, S. C., Blain, A. W., Smail, I., & Ivison, R. J. 2005, ApJ, 622, 772

Chary, R. & Elbaz, D. 2001, ApJ, 556, 562

Choi, P. I. et al. 2006, ApJ, 637, 227

Cimatti, A. et al. 2002, A&A, 391, 1

Condon, J. J., Cotton, W. D., Yin, Q. F., Shupe, D. L., Storrie-Lombardi, L. J., Helou, G., Soifer, B. T., & Werner, M. W. 2003, AJ, 125, 241

Cowie, L., Songaila, A., Hu, E. M., & Cohen, J. G. et al. 1996, AJ, 112, 839

Dahlen, T., Mobasher, B., Dickinson, M., Ferguson, H. C., Giavalisco, M., Kretchmer, C., & Ravindranath, S. 2007, ApJ, 654, 172

Drory, N., Bender, R., Feulner, G., Hopp, U., Maraston, C., Snigula, J., & Hill, G. J. 2004, ApJ, 608, 742

Drory, N., Salvato, M., Gabasch, A., Bender, R., Hopp, U., Feulner, G., & Pannella, M. 2005, ApJL, 619, 131

Egami, E. et al. 2004, ApJS, 154, 130

Fadda, D., Jannuzi, B. T., Ford, A., & Storrie-Lombardi, L. J. 2004, AJ, 128, 1

Fadda, D. et al. 2006, AJ, 131, 2859

Fazio, G. G. et al. 2004, ApJS, 154, 10

Förster-Schreiber, N. M. et al. 2004, ApJ, 616, 40

Foucaud, S., McCracken, H. J., Le Fevre, O., Arnouts, S., Brodwin, M., Liily, S. J., Crampton, D., & Mellier, Y. 2003, A&A, 409, 835

Franx, M. et al. 2003, ApJL, 587, 79

Frayer, D. T. et al. 2006, AJ, 131, 250

Giavalisco, M. 2002, ARA&A, 40, 579

Heavens, A., Panter, B., Jimenez, R., & Dunlop, J. 2004, Nature, 428, 625

Hildebrandt, H. et al. 2005, A&A, 441, 905

Hildebrandt, H., Pielorz, J., Erben, T., Schneider, P., Eifler, T., Simon, P., & Dietrich, J. P. 2007, A&A, 462, 865

Hopkins, A. M. 2004, ApJ, 615, 209

Huang, J.-S. et al. 2004, ApJS, 154, 44

Huang, J.-S. et al. 2005, ApJ, 634, 137

Hunt, M. P., Steidel, C. C., Adelberger, K. L., & Shapley, A. E. 2004, ApJ, 605, 625

Im, M., Simard, L., Faber, S. M., Koo, D. C., Gebhardt, K., Wilmer, C. N. A., Phillips, A., Illingworth, G., Vogt, N. P., & Sarajedini, V. L. 2002, ApJ, 571, 136

Ivison, R. J. et al. 2004, ApJS, 154, 124

Juneau, S. et al. 2005, ApJL, 619, 135

Kennicutt, R. 1998, ARA&A, 36, 189

Kodama, T. et al. 2004, MNRAS, 350, 1005

Labbé, I. et al. 2005, ApJL, 624, 81

Lacy, M. et al. 2005 ApJS, 161, 41

Lilly, S. J., Tresse, L., Hammer, F., Crampton, D., & Le Fevre, O. 1995, ApJ, 455, 108

Lutz, D., Vallante, E., Sturm, E., Genzel, R., Tacconi, L. J., Lehnert, M. D., Sternberg, A., & Baker, A. J. 2005, ApJL, 625, 83

Madau, P. 1995, ApJ, 441, 18

McLure, R. J. et al. 2006, MNRAS, 372, 357

Menéndez-Delmestre, K. et al. 2007, ApJL, 655, 65

Meurer, G. R., Heckman, T. M., & Calzetti, D. 1999, ApJ, 521, 64

Nagamine, K., Cen, R., Hernquist, L., Ostriker, J. P., & Springel, V. 2005, ApJ, 618, 23

Neistein, E., van den Bosch, F. C., & Dekel, A. 2006, MNRAS, 372, 933

Ouchi, M. et al. 2004 ApJ, 611, 660

Panter, B., Jimenez, R., Heavens, A. F., & Charlot, S. (astro-ph/0608531)

Papovich, C., Dickinson, M., & Ferguson, H. C. 2001, ApJ, 559, 620

Papovich, C. 2006, NewAR, 50, 134

Peebles, P. J. E. 1975, ApJ, 196, 647

Reddy, N. A., Steidel, C., C., Fadda, D., Yan, L., Pettini, M., Shapley, A. E., Erb, D. K., & Adelberger, K. L. 2006, ApJ, 644, 792

Rieke, G. H. et al. 2004, ApJS, 154, 25

Rigopoulou, D. et al. 2006, ApJ, 648, 81

Saracco, P. et al. 2004, A&A, 420, 125

Sawicki, M., & Webb, T. M. A. 2005, ApJL, 618, 67

Schiminovich, D. et al. 2005, ApJL, 619, 47

Schmidt, M. 1968, ApJ., 151, 393

Shapley, A. E., Steidel, C. C., Adelberger, K. L., Dickinson, M., Giavalisco, M., & Pettini, M. 2001, ApJ, 562, 95

Shapley, A. E., Steidel, C. C., Erb, D. K., Reddy, N. A., Adelberger, K. L., Pettini, M., Barmby, P., & Huang, Jiasheng, 2005, ApJ, 626, 698

Shim, H., Im, M., Pak, S., Choi, P., Fadda, D., Helou, G., & Storrie-Lombardi, L. 2006, ApJS, 164, 435

Simcoe, R. A., Metzger, M. R., Small, T. A., & Araya, G. 2000, AAS, 196, 5209

Smail, I., Ivison, R. J., Blain, A. W., & Kneib, J.-P. 2002, MNRAS, 331, 495

Steidel, C. C., & Hamilton, D. 1993, AJ, 105, 2017

Steidel, C., Adelberger, K. L., Giavalisco, M., Dickinson, M., & Pettini, M. 1999, ApJ, 519, 1

Steidel, C. C., Adelberger, K. L., Shapley, A. E., Pettini, M., Dickinson, M., & Giavalisco, M. 2003, ApJ, 592, 728

Telesco, C. M., & Harper, D. A. 1980, ApJ, 235, 392

Tecza, M. et al. 2004, ApJL, 605, 109

Thomas, D., Maraston, C., Bender, R., & Mendes de Oliveira, C. 2005, ApJ, 621, 673

Williams, L. L. R. & Lewis, G. F. 1996, MNRAS, 281, 35

Witt, A. N. & Gordon, K. D. 2000, ApJ, 528, 799

van Dokkum, P. G. et al. 2006, ApJL, 638, 59

Yan, L. et al. 2004, ApJS, 154, 60